Myosins XI Are Involved in Exocytosis of Cellulose Synthase Complexes[1][OPEN]

Weiwei Zhang,[a,2] Chao Cai,[a,2] and Christopher J. Staiger[a,b,3,4]

[a]Department of Biological Sciences, Purdue University, West Lafayette, Indiana 47907-2064

[b]Department of Botany and Plant Pathology, Purdue University, West Lafayette, Indiana 47907

ORCID IDs: 0000-0002-4754-6241 (W.Z.); 0000-0002-6547-259X (C.C.); 0000-0003-2321-1671 (C.J.S.).

In plants, cellulose is synthesized at the cell surface by plasma membrane (PM)-localized cellulose synthase (CESA) complexes (CSCs). The molecular and cellular mechanisms that underpin delivery of CSCs to the PM, however, are poorly understood. Cortical microtubules have been shown to interact with CESA-containing compartments and mark the site for CSC delivery, but are not required for the delivery itself. Here, we demonstrate that myosin XI and the actin cytoskeleton mediate CSC delivery to the PM by coordinating the exocytosis of CESA-containing compartments. Measurement of cellulose content indicated that cellulose biosynthesis was significantly reduced in a *myosin xik xi1 xi2* triple-knockout mutant. By combining genetic and pharmacological disruption of myosin activity with quantitative live-cell imaging, we observed decreased abundance of PM-localized CSCs and reduced delivery rate of CSCs in myosin-deficient cells. These phenotypes correlated with a significant increase in failed vesicle secretion events at the PM as well as an abnormal accumulation of CESA-containing compartments at the cell cortex. Through high-resolution spatiotemporal assays of cortical vesicle behavior, we identified defects in CSC vesicle tethering and fusion at the PM. Furthermore, disruption of myosin activity reduced the delivery of several other secretory markers to the PM and reduced constitutive and receptor-mediated endocytosis. These findings reveal a previously undescribed role for myosin in vesicle secretion and cellulose production at the cytoskeleton-PM-cell wall nexus.

Cellulose microfibrils are the major load-bearing component of the plant cell wall and play essential roles in plant growth and development (McFarlane et al., 2014; Wallace and Somerville, 2015). Cellulose is produced at the plasma membrane (PM) by multimeric cellulose synthase complexes (CSCs), or rosettes, consisting of multiple cellulose synthase (CESA) proteins (Delmer, 1999; Somerville, 2006). Both freeze-fracture studies and live-cell quantitative imaging indicate that CSCs are assembled in Golgi (Giddings et al., 1980; Haigler and Brown, 1986; Paredez et al., 2006). CSCs are also present in small cytoplasmic CESA compartments (Gutierrez et al., 2009) or microtubule-associated transport vesicles (MASCs; Crowell et al., 2009), which are associated with CSC delivery, generated by endocytosis, or both. Understanding the intracellular trafficking and delivery of CSCs is of great importance, as it determines the abundance of CSCs at the PM and consequently affects the amount of cellulose produced and assembled in the cell wall (Bashline et al., 2014; Wallace and Somerville, 2015).

The cytoskeleton is implicated as a central player that coordinates trafficking of CSCs. In addition to choreographing the trajectory of CSCs in the PM, cortical microtubules interact with MASCs through the linker protein CELLULOSE SYNTHASE INTERACTIVE1 and mark the sites for insertion of newly delivered CSCs (Paredez et al., 2006; Gutierrez et al., 2009; Bringmann et al., 2012; Zhu et al., 2018). However, they do not influence the rate of CSC delivery or abundance of CSCs at the PM, and cellulose content is not altered after treatment with the microtubule-disrupting drug oryzalin (Paredez et al., 2006; Gutierrez et al., 2009; Sampathkumar et al., 2013). By contrast, the actin cytoskeleton has recently been shown to participate in the delivery and endocytosis of CSCs, thereby affecting the amount of cellulose produced. Small cytoplasmic CESA compartments are observed along subcortical actin filaments and translocate in an actin-dependent fashion (Sampathkumar et al., 2013). Genetic disruption of actin cytoskeleton organization in the *act2 act7* mutant or pharmacological perturbation with the actin

polymerization inhibitor latrunculin B (LatB) leads to significant inhibition of the rate of delivery of CSCs to the PM and a marked reduction in overall cellulose content (Sampathkumar et al., 2013). Despite these intriguing results, the molecular and cellular mechanisms that underpin a role for actin in vesicle delivery and CSC membrane dynamics remain unresolved.

In plant cells, a highly dynamic cortical actin network comprising single filaments and actin filament bundles is coordinated by a plethora of conserved and novel actin-binding proteins (Li et al., 2015). Myosins are molecular motors that transport diverse cargo along actin filaments and, in plants, are grouped into class XI and class VIII subfamilies (Reddy and Day, 2001; Perico and Sparkes, 2018; Ryan and Nebenführ, 2018). In Arabidopsis (*Arabidopsis thaliana*), class XI contains 13 isoforms that share functional redundancy (Peremyslov et al., 2008). Based on analysis of Arabidopsis mutants with two, three, or four of the most highly expressed myosin XI genes knocked out, these motors are implicated in regulating actin organization and dynamics and are key contributors to organelle and vesicle motility (Prokhnevsky et al., 2008; Peremyslov et al., 2010, 2012; Ueda et al., 2010; Cai et al., 2014; Madison et al., 2015). The velocity of myosin translocation along actin filaments, and therefore the rate of cytoplasmic streaming, also correlates with rates of cell expansion and plant growth (Tominaga et al., 2013). When chimeric myosins with faster or slower motor domains compared to an endogenous myosin XI are expressed in transgenic Arabidopsis plants, the fast myosin supports larger epidermal cells and larger plants, whereas slow myosin leads to shorter cells and smaller plants (Tominaga et al., 2013). At present, it is not known how the velocity of chimeric myosins affects axial cell expansion or whether this involves differences in cell wall composition and assembly.

In animal and yeast cells, actin and myosin are shown to participate in exocytosis and membrane fusion. For example, actin remodeling and/or polymerization correlates with increased vesicle secretion (Gutiérrez, 2012). In some systems, actin coats the secretory compartments and, together with myosin II, stabilizes the fusion pore or regulates the rate of fusion pore expansion (Nightingale et al., 2012). Furthermore, myosin V motors interact directly with Rab GTPases and the exocyst complex to facilitate secretory vesicle trafficking (Jin et al., 2011; Donovan and Bretscher, 2012). In plant cells, the function of actin and myosin in these processes has not been established. Arabidopsis MYOSIN XIK mediates the motility of several secretory vesicle markers, including the Rab GTPase RabA4b, SECRETORY CARRIER MEMBRANE2, and the SYNTAXIN OF PLANTS41 (SYP41), and a functional XIK-YFP (yellow fluorescent protein) partially colocalizes with RabA4b and SECRETORY CARRIER MEMBRANE2 compartments (Avisar et al., 2012; Peremyslov et al., 2012; Park and Nebenführ, 2013). A proteomics study in Arabidopsis identified both CESA

and myosin XI in compartments enriched for the RabD2a/ARA5 marker, a Rab GTPase that decorates Golgi, trans-Golgi network (TGN)/early endosomes (EE), and post-Golgi vesicles (Heard et al., 2015). However, other than vesicle motility, it is not known whether myosin XI also regulates secretion or fusion to the PM.

In this study, we combined genetic and pharmacological approaches with quantitative live-cell imaging to investigate the role of myosin in CESA trafficking and CSC secretion. We demonstrated that cortical actin and myosin play a prominent role in vesicle exocytosis and are responsible for trafficking of CESA-containing compartments through tethering or insertion of CSCs at the PM.

RESULTS

Cellulose Content Is Reduced in the *myosin xi3KO* Mutant

An Arabidopsis *myosin xi1 xi2 xik* triple-knockout mutant exhibits an overall dwarf plant phenotype with shorter cell lengths in both dark-grown hypocotyls and light-grown roots, resembling features that are typical of cellulose-deficient mutants and mimicking chemical inhibition of cellulose synthesis (Fagard et al., 2000; Peremyslov et al., 2010; Cai et al., 2014; Bashline et al., 2015). Although cellulose production involves intracellular trafficking and exocytosis of CSCs (Zhu et al., 2018), indications that myosin XI motors could be responsible are limited. To test whether myosin participates in cellulose production, we measured cellulose content in the previously characterized triple-knockout mutant, hereafter referred to as *xi3KO* (Peremyslov et al., 2010). Cellulose content in alcohol-insoluble cell wall fractions of seedlings was determined after hydrolysis of all noncellulosic material in acetic-nitric (AN) reagent (Updegraff, 1969); alternatively, hydrolysis in 2 M trifluoroacetic acid (TFA) yields insoluble crystalline cellulose equivalent in amount to the AN reagent but allows recovery of noncellulosic monosaccharides including Glc from amorphous cellulose (Gibeaut and Carpita, 1991). The *xi3KO* mutant had significantly reduced total and crystalline cellulose compared to the wild-type control (Fig. 1). Similarly, wild-type seedlings grown on medium containing LatB showed a decrease in cellulose content (Fig. 1), consistent with a previous study (Sampathkumar et al., 2013). Furthermore, seedlings grown on medium containing the plant myosin inhibitor 2,3-butanedione monoxime (BDM) also had significantly reduced cellulose (Supplemental Figure S1).

We also analyzed cell wall monosaccharide composition to determine if noncellulosic cell wall components were altered. No major differences in amounts of individual monosaccharides were detected in the cell wall fractions from seedlings of the *xi3KO* mutant or those treated with LatB compared to those of the wild type (Supplemental Table S1).
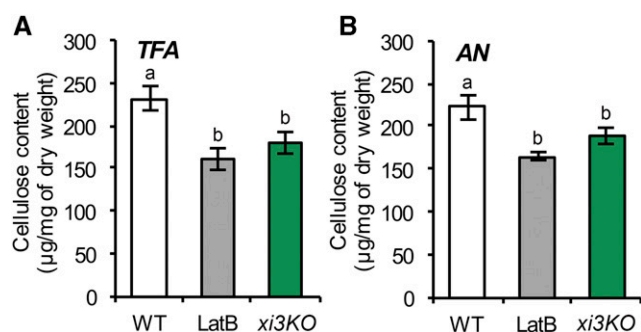
Figure 1. Cellulose content is reduced in the *myosin xi3KO* mutant. Ethanol-insoluble cell wall material (CWM) was prepared from 5-d-old etiolated hypocotyls of wild-type (WT) seedlings, the *myosin xi3KO* mutant, and wild type growing on plates containing 100 nM latrunculin B (LatB). A and B, Cellulose content was measured as described in the "Materials and Methods." The noncellulosic component of CWM was hydrolyzed with 2 M trifluoroacetic acid (TFA; A) or acetic nitric reagent (AN; B) and the insoluble residue used for total cellulose determination. The TFA method was used for total cellulose determination and the AN method for crystalline cellulose determination. Cellulose content was significantly reduced in LatB-treated and *xi3KO* mutant hypocotyls compared to wild type. Values given are means ± SE ($n = 4$; one-way ANOVA with Tukey's post-hoc test, letters [a and b] denote sample/groups that show statistically significant differences from other groups, $P < 0.05$).

Pentabromopseudilin Is a Potent Myosin Inhibitor in Plant Cells

To investigate the role of myosin in cellulose deposition in detail, we used a pharmacological approach to acutely inhibit the activity of myosins. This further serves to bypass the potential genetic redundancy due to the presence of multiple myosin XI proteins in Arabidopsis, as well as possible indirect effects resulting from long-term disruption of myosin activity in higher-order mutants. BDM is the most commonly used plant myosin inhibitor; however, it requires a high concentration, and its specificity has been questioned (McCurdy, 1999; Tominaga et al., 2000; Funaki et al., 2004). To search for additional plant myosin inhibitors, we screened chemical inhibitors of class V myosins, which are related to plant myosins VIII and XI (Foth et al., 2006). Pentabromopseudilin (PBP) and MyoVin-1 potently inhibit myosin V in animal and fungal cells (Fedorov et al., 2009; Islam et al., 2010).

To test whether these two inhibitors target plant myosins, we measured Golgi motility as a myosin XI-dependent process (Prokhnevsky et al., 2008; Peremyslov et al., 2010). Etiolated hypocotyl epidermal cells expressing YFP fused to mannosidase I, a Golgi resident enzyme that serves as a Golgi marker (Nebenführ et al., 1999), were imaged by time-lapse variable-angle epifluorescence microscopy. After 15-min inhibitor treatment, fast directional and long-distance movement of Golgi was detected in mock and MyoVin-1-treated cells (Fig. 2, A and B; Supplemental Movie S1). By contrast, rapid and directional Golgi movement was markedly reduced in

BDM- and PBP-treated cells, with most organelles moving slowly or wiggling in place (Fig. 2, A and B; Supplemental Movie S1). Quantitative analyses showed a significant reduction in average Golgi velocity after BDM and PBP treatment compared to control cells or those treated with MyoVin-1 (Fig. 2C). Plant Golgi display both fast directional and slow wiggling movement patterns (Akkerman et al., 2011). PBP appeared to inhibit both types of movement, whereas BDM mainly impacted the fast-moving population with a velocity greater than 1 μm s^{-1} (Supplemental Fig. S2). Moreover, we found that inhibition of Golgi motility by PBP was both time and dose dependent, and the drug could be washed out of cells to restore motility (Supplemental Fig. S3, A–C).

To test the effects of these inhibitors on myosin-based motility more directly, we took advantage of a functional, full-length MYOSIN XIK fused with YFP (XIK-YFP; Peremyslov et al., 2012). This reporter associates with small vesicle clusters that traffic along F-actin and appear as "beads-on-a-string" (Peremyslov et al., 2012). We measured velocities of these vesicles after inhibitor treatment using time-lapse images collected with spinning-disk confocal microscopy (SDCM). In mock-treated cells, the XIK-YFP vesicles moved at a mean speed of ~5 μm s^{-1}, whereas mean velocities decreased by nearly 80% in PBP-treated cells (Fig. 2, D–F; Supplemental Movie S2). By contrast, mean velocities decreased by only 10% upon BDM treatment and less than 5% with MyoVin-1 treatment (Fig. 2, D–F; Supplemental Movie S2). The reason that BDM did not strongly inhibit XIK-YFP motility could be that it has a lower specificity in targeting the XIK isoform. Finally, PBP showed a dose- and time-dependent inhibition of XIK-YFP motility and the drug could be washed out of cells to restore motility (Supplemental Fig. S3, D–F).

Myosin XI in the green alga *Chara corallina* has the fastest velocity reported among all myosin motors (~50 μm s^{-1}) and drives rapid cytoplasmic streaming (Yamamoto et al., 1994; Shimmen and Yokota, 2004). PBP inhibited the velocity of cytoplasmic streaming in internodal cells of *C. corallina* by ~75% after 15-min treatment with 1 μM PBP and the inhibition was both dose and time dependent (Supplemental Fig. S4). These data demonstrate that PBP effectively inhibits myosin-dependent organelle motility and validate its use as a myosin inhibitor in plants. By contrast, MyoVin-1 did not inhibit any plant myosin-dependent process tested here (Supplemental Table S2) and will not be used further.

Abundance of CSCs in the PM Is Reduced in the *xi3KO* Mutant

One explanation for the reduced cellulose content in *xi3KO* could be that the number of CSCs in the PM is decreased. To address this possibility, a line expressing YFP-CESA6 in the *prc1-1* homozygous mutant background (Paredez et al., 2006) was crossed with the *xi3KO* mutant. We recovered *myosin xi* triple-homozygous
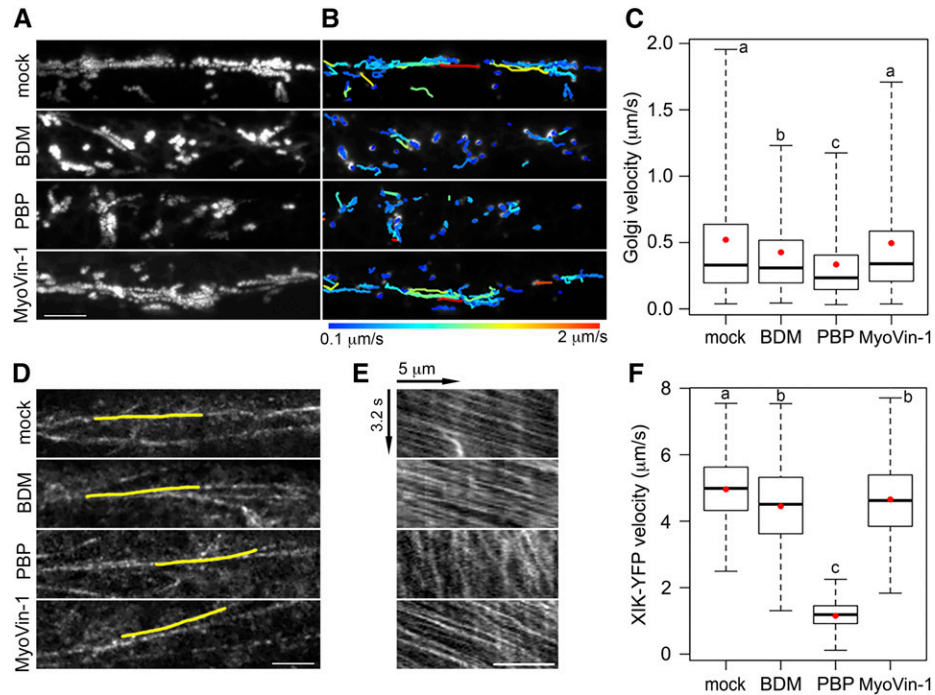
Figure 2. Myosin inhibitor treatments reduce motility in hypocotyl epidermal cells. A, Representative time projections show the trajectories of Golgi motility from apical epidermal cells of 3-d-old etiolated hypocotyls expressing YFP-Mannosidase I. Seedlings were treated for 15 min with mock (0.2% DMSO), 30 mм 2,3-butanedione monoxime (BDM), 10 μM pentabromopseudilin (PBP), or 20 μM MyoVin-1 followed by imaging with variable-angle epifluorescence microscopy. Time projections were generated with maximum intensity of 61 frames collected at 0.5-s intervals. Bar, 10 μm. B, Trajectories of Golgi motility detected with the ImageJ plug-in "TrackMate" for images shown in A. Heat map of trajectories indicate the average speed from 0.1 to 2 μm s^{-1}. C, Box-whisker plots show average velocity of Golgi in inhibitor-treated epidermal cells. Red circles show the mean velocity. The rate of average Golgi velocity was significantly decreased after BDM and PBP treatments, whereas MyoVin-1 had little or no effect. Values given are means $\pm$ SE ($n > 3,000$ trajectories from 10 hypocotyls per treatment; one-way ANOVA with Tukey's post-hoc test, $P < 0.001$). D, Representative single-frame images of the cortical cytoplasm in hypocotyl epidermal cells expressing MY-OSIN XIK-YFP imaged with spinning-disk confocal microscopy (SDCM). Etiolated seedlings were treated with inhibitors for 15 min, followed by time-lapse imaging using an 80-ms interval for 41 frames. Bar, 5 μm. E, Kymographs of the yellow lines depicted in D show fast movement of the vesicles over a 3.2-s time span. Bar, 5 μm. F, Quantification of XIK-YFP velocity from analysis of multiple kymographs. The motility of YFP-XIK was markedly decreased in PBP-treated cells and slightly reduced in BDM or MyoVin-1-treated cells compared to mock treatment. Values given are means $\pm$ SE ($n > 500$ tracks from 10 hypocotyls per treatment; one-way ANOVA with Tukey's post-hoc test, letters [a–c] denote samples/groups that show statistically signifcant differences from other groups, $P < 0.001$).

knockouts as well as wild-type siblings expressing YFP-CESA6 in the presence of *prc1-1*. When examined by SDCM, the density of CSCs at the PM in the *xi3KO* mutant was reduced by greater than 30% compared to wild-type siblings (Fig. 3, A–C). We also performed short-term treatment of wild-type siblings with BDM and PBP to test whether acute inhibition of myosin activity could recapitulate the reduction of CSC density in the *xi3KO* mutant. After BDM and PBP treatment for 15 min, the density of PM-localized CSCs dropped significantly by 14% and 25%, respectively, compared to that of nontreated cells (Fig. 3, A–C). By contrast, treatment with LatB at a high concentration (10 μM) had no effect on CSC density (Fig. 3, A–C); the latter result was consistent with a previous report (Sampathkumar et al., 2013). The motility of CSCs in the plane of PM was also reduced in the *xi3KO* mutant and BDM- and PBP-treated cells, but not in LatB-treated cells (Fig. 3, D–F).

The pattern of CESA distribution at the PM correlates with the position of Golgi in the cortical cytoplasm, and disruption of the actin cytoskeleton reportedly causes clustering of CESA-containing Golgi bodies and, consequently, uneven distribution of CSCs at the PM (Gutierrez et al., 2009; Sampathkumar et al., 2013). We observed similar patterns in LatB-treated cells, whereas in *xi3KO* or cells treated with BDM or PBP, apparent Golgi clustering or patchy distribution of CSCs at the PM was not detected frequently (Supplemental Fig. S5). In support of these observations, we quantified the percentage of single Golgi bodies in the cell cortex as an indicator of the level of Golgi clustering. In LatB-treated cells, there was a significantly lower proportion of single Golgi compared with the wild type, confirming a high extent of Golgi clustering, whereas in *xi3KO* and BDM- and PBP-treated cells, the proportion of single Golgi increased significantly compared with controls
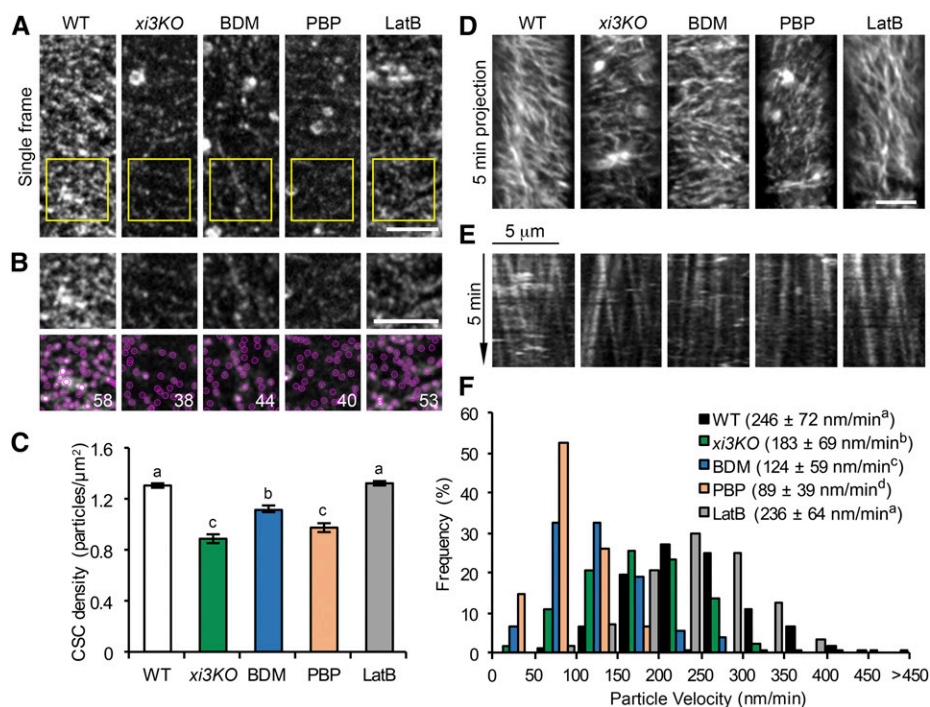
Figure 3. The density and motility of CSC particles at the plasma membrane are reduced in myosin-deficient cells. Etiolated hypocotyl epidermal cells of *xi3KO* or wild-type (WT) siblings expressing YFP-CESA6 were imaged with SDCM. Seedlings were pretreated with mock (0.2% DMSO), 30 mM BDM, 10 μM PBP, or 10 μM LatB for 15 min. A, Representative single-frame images show the distribution of CSCs at the PM. Bar, 5 μm. B, Selected regions (yellow box) in A were magnified and CSC particles detected (marked in magenta). The number of particles in each region is shown in white. Bar, 5 μm. C, Quantitative analysis shows that the density of CSCs at the PM was significantly reduced in *xi3KO* or after BDM and PBP treatment, but not in LatB-treated cells. Values given are means ± SE ($n \geq 35$ cells from 10 hypocotyls per treatment; more than 12,000 particles were measured from total areas of > 9,400 μm² in wild-type, *xi3KO*, and BDM-, PBP-, and LatB-treated cells (one-way ANOVA with Tukey's post-hoc test, $P < 0.01$). D, Representative time projections show the trajectories of CSCs at the PM. Time projections were generated by average intensity with 61 frames collected at 5-s intervals. Bar, 5 μm. E, Representative kymographs show the movement of CSCs during a 5-min interval. F, Quantitative analysis shows the distribution and average velocities of CSCs. The average CSC velocities in *xi3KO* and BDM- and PBP-treated cells were greatly reduced compared to wild-type or LatB-treated cells. Values given are means ± SD ($n > 500$ CSC trajectories per treatment, one-way ANOVA with Tukey's post-hoc test, letters [a–d] denote samples/groups that show statistically significant differences from other groups, $P < 0.05$).

(Supplemental Fig. S5). This indicates that, in contrast to actin, disruption of myosin does not cause clustering of cortical Golgi, and the decrease of CSC density at the PM in myosin-deficient cells is unlikely a result of disruption of Golgi distribution.

Rate of Delivery of CSCs to the PM Is Determined by Myosin

The decreased density of CSCs in myosin-deficient cells indicates that myosin may be required for the delivery of CSCs to the PM. Fluorescence recovery after photobleaching (FRAP) experiments have been developed to analyze the rate of delivery of CSCs to the PM (Gutierrez et al., 2009; Bashline et al., 2013; Sampathkumar et al., 2013; Luo et al., 2015).

To test the role of myosin, we performed FRAP experiments on the *xi3KO* mutant expressing YFP-CESA6 as well as on inhibitor-treated wild-type hypocotyl epidermal cells. In brief, a small region was irradiated to minimize the bleaching of the cytoplasmic mobile CESA pool, and a central subregion was selected to avoid error introduced by migration of CSCs into the measured region (Fig. 4A). For inhibitor studies, to minimize the duration of treatment, we did not pretreat hypocotyls but instead mounted them directly in inhibitor solution and immediately began time-lapse imaging. It has been reported that the rate of CSC delivery correlates with the abundance of underlying CESA-containing Golgi, and choosing a bleached region with few Golgi will affect the apparent delivery frequency (Gutierrez et al., 2009; Sampathkumar et al., 2013). To reduce the chances of biasing our analysis toward regions of PM that were deficient in CSC delivery due to a lack of nearby Golgi, we avoided regions that had few CSC particles or few Golgi. This was confirmed by analyzing the density of CSCs in regions selected for photobleaching, and no significant difference was detected between any genotype or treatment (Supplemental Fig. S6).
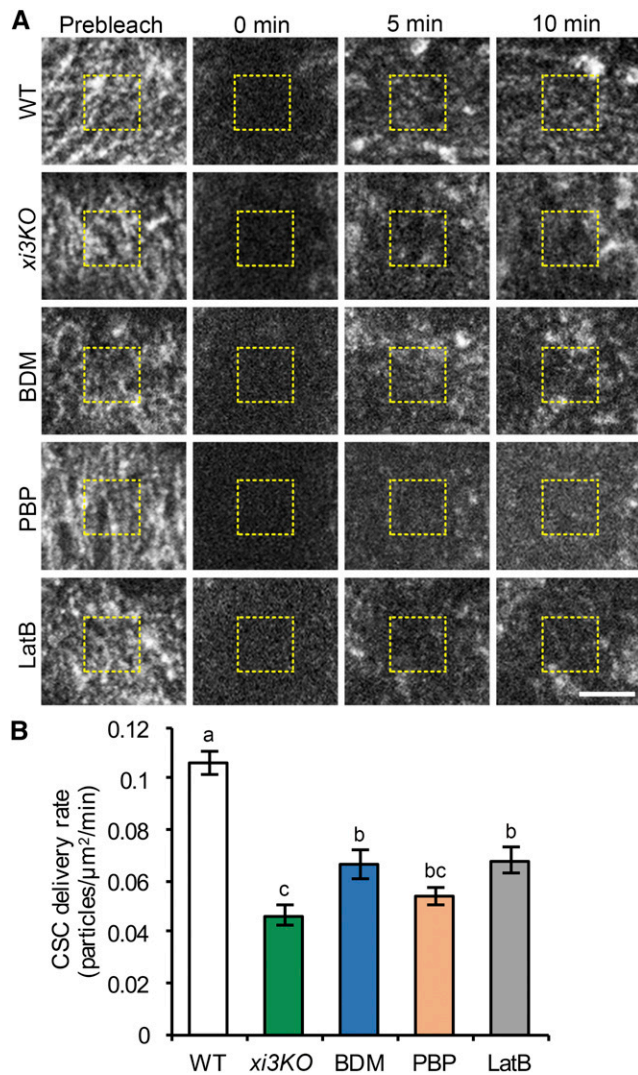
Figure 4. Delivery of CSCs to the PM is reduced in myosin-deficient cells. A, Representative single-frame images of PM-localized CSC particle recovery after photobleaching. Seedlings of wild type (WT) or *xi3KO* were mounted in mock (0.2% DMSO), 30 mm BDM, 10 μM PBP, or 10 μM LatB just prior to imaging. A region of interest at the PM was photobleached and the number of newly delivered CSCs was counted in a subarea within the region (yellow dashed box). Bar, 5 μm. B, The rate of delivery of CSCs to the PM was calculated from the total number of newly delivered CSCs during the initial 5 min of recovery divided by the measured area and time. The CSC delivery was significantly inhibited in *xi3KO* and BDM-, PBP-, and LatB-treated cells compared with mock-treated wild-type sibling. Values given are means ± SE ($n \geq$ 11 cells per genotype or treatment, one-way ANOVA with Tukey's post-hoc test, letters [a–c] denote samples/groups that show statistically significant differences with other groups, $P < 0.05$).

After photobleaching, we observed gradual recovery of CSCs in all genotypes or treatments; however, the rate of recovery in *xi3KO* and BDM-, PBP-, and LatB-treated cells was reduced compared with the wild type (Fig. 4A). We quantified the newly delivered CSC particles in the bleached region according to published methods, and only de novo appearances of particles

that exhibited a static phase followed by steady migration were counted as new delivery events (Gutierrez et al., 2009). Mock-treated wild-type cells had a delivery rate of 0.11 ± 0.02 particles μm^{-2} min^{-1} (Fig. 4B). By contrast, the CSC delivery rate in the *xi3KO* mutant decreased by greater than 50% (Fig. 4B). In BDM-, PBP-, and LatB-treated cells, the delivery rates were reduced by 37%, 48%, and 36%, respectively (Fig. 4B). The reduced rate of delivery of CSCs in both *xi3KO* and myosin inhibitor-treated cells indicates that myosin is involved in delivery or insertion of CESA at the PM.

To verify that cortical microtubules do not affect that rate of delivery of CSCs (Gutierrez et al., 2009), we pretreated seedlings with oryzalin for 2 h, which destabilized the majority of microtubules (Supplemental Fig. S7A). FRAP analysis of oryzalin-treated cells showed that the CSC delivery rate was not significantly different compared to control cells (Supplemental Fig. S7, B and C).

We also tested whether the actin-myosin transport network mediates delivery of general cargo proteins to the PM, in addition to CESA. We obtained two well-characterized protein markers, the auxin efflux carrier PINFORMED2 (PIN2) and the brassinosteroid receptor BRASSINOSTEROID INSENSITIVE1 (BRI1), which are actively delivered to the PM through de novo secretion or endomembrane recycling (Geldner et al., 2007; Luschnig and Vert, 2014). Treatment of roots expressing PIN2-GFP (green fluorescent protein) or BRI1-GFP with BDM, PBP, or LatB for 2 h revealed significantly reduced fluorescence intensity at the PM, compared with that in mock-treated cells (Supplemental Fig. S8, A, B, D, and E). The decreased PM fluorescence intensity correlated with an increased number of intracellular compartments (Supplemental Fig. S8, A and B), suggesting that the delivery of PIN2-GFP and BRI1-GFP to the PM was inhibited and the proteins were retained intracellularly after myosin or actin inhibitor treatment. In addition, treatment of cells expressing the secretory marker secGFP (Zheng et al., 2004) with BDM and PBP caused a significant retention of secGFP signal inside the cell, compared with complete secretion out of the cell in mock-treated cells (Supplemental Fig. S8, C and F). Collectively, our results indicate that myosin activity is required for general protein secretion, including delivery of CSCs to the PM.

CESA Compartments Accumulate in the Cortical Cytoplasm after Myosin Disruption

Small cytoplasmic CESA-containing compartments or vesicles observed at the cell cortex are likely to be associated with delivery of CSCs to the PM through a poorly defined mechanism (Crowell et al., 2009; Gutierrez et al., 2009; Wallace and Somerville, 2015). Previous work showed association of CESA compartments with actin filaments in the subcortical cytoplasm (Sampathkumar et al., 2013). We tested whether myosin XI functions in trafficking of CESA compartments to

the PM for CSC delivery. When we combined 0.2 μm SDCM optical sections into cortical (0 to 0.4 μm below the PM) and subcortical (0.6 to 1 μm below the PM) cytoplasm (Sampathkumar et al., 2013), we found that the abundance of cytoplasmic CESA compartments in the cortical cytoplasm increased more than 2-fold over wild-type cells in the *xi3KO* mutant or after acute treatment with BDM or PBP (Fig. 5). Treatment with LatB also increased the number of cortical CESA compartments to a similar level (Fig. 5). By contrast, the number of subcortical CESA compartments was either unchanged or was modestly increased upon drug treatment (Fig. 5).

An increased abundance of cortical MASCs has been observed in cells treated with cellulose synthesis inhibitors (e.g. isoxaben) or osmotic stress (Crowell et al.,

2009; Gutierrez et al., 2009). Under these conditions, CSCs were mostly depleted from the PM and internalized into MASCs, which were tethered to cortical microtubules and displayed stationary or steady microtubule tip-tracking motility with an average velocity of ~4 μm min^{-1} (Crowell et al., 2009; Gutierrez et al., 2009; Sampathkumar et al., 2013; Lei et al., 2015). By contrast, the accumulated CESA compartments we observed in myosin- and actin-deficient cells exhibited high dynamicity (Supplemental Movie S3). Most of the compartments displayed erratic or diffuse movement with mean velocities greater than 7 μm min^{-1} in all genotypes or inhibitor treatments, and we did not observe the stationary or microtubule-dependent motility pattern of CESA compartments in the cell cortex (Supplemental Fig. S9, A and C; Supplemental Movie
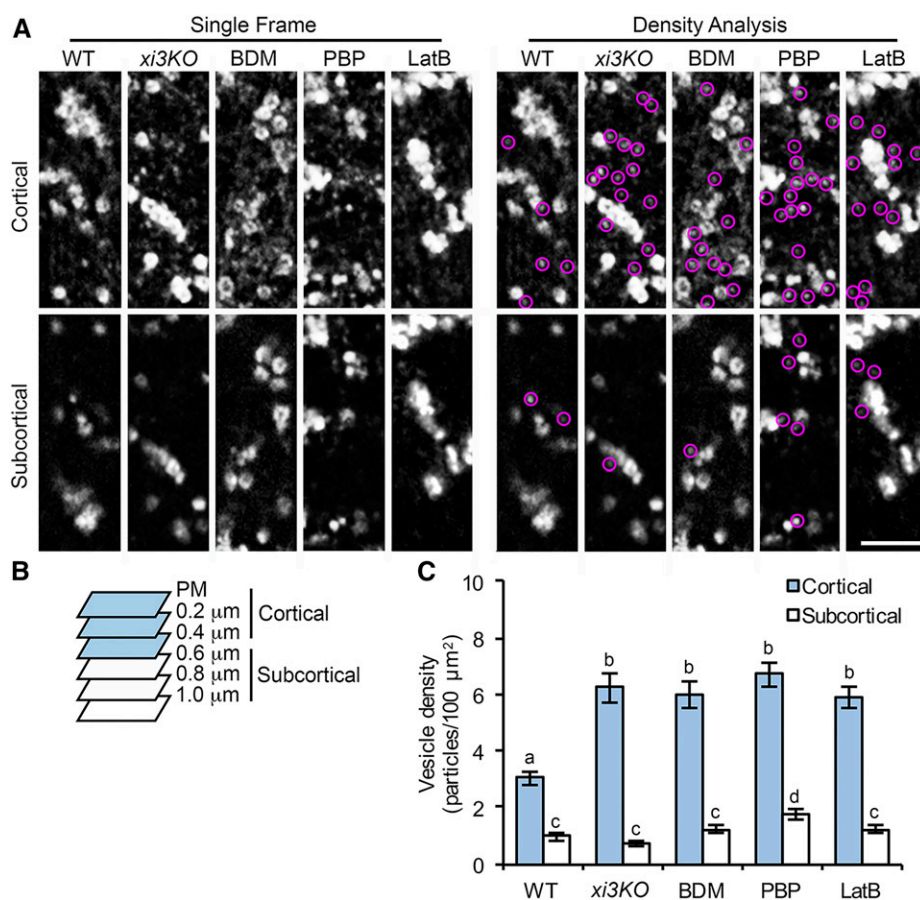

Figure 5. The density of small CESA compartments is increased in the cell cortex following myosin inhibition. A, Representative single frames taken at cortical and subcortical focal planes in hypocotyl epidermal cells. Seedlings of *xi3KO* or wild-type (WT) siblings expressing YFP-CESA6 were treated with mock (0.2% DMSO), 30 mM BDM, 10 μM PBP, or 10 μM LatB for 15 min prior to imaging. The cytoplasmic CESA compartments are highlighted with magenta circles. Bar, 5 μm. B, Diagram shows that optical sections of 0.2-μm step size were taken by SDCM starting at the PM. Focal planes from the PM to 0.4 μm below the PM were defined as cortical cytoplasm and from 0.6 μm to 1.0 μm were defined as subcortical cytoplasm. C, Quantitative analysis of vesicle density shows that the number of CESA compartments was increased significantly in the cortical but not the subcortical cytoplasm in *xi3KO* and BDM-, PBP-, and LatB-treated cells. Values given are means ± SE ($n \geq 20$ cells from 10 seedlings for each genotype or treatment; a total of 333, 567, 790, 686, and 602 compartments were measured from total areas of 8,344, 8,418, 11,229, 8,321, and 8,041 μm^2 in wild-type, *xi3KO*, and BDM-, PBP-, and LatB-treated cells, respectively; one-way ANOVA with Tukey's post-hoc test; letters [a–d] denote samples/groups that show statistically significant differences with other groups, $P < 0.05$).

S3). The motility pattern of those compartments suggests that they were not the same population as the MASCs observed in cells treated with isoxaben or in cells under stress. In addition, inhibition of myosin or actin only reduced the fast-moving population of CESA compartments (>20 μm/min) in both cortical and subcortical cytoplasm, but not those that had a lower motility (Supplemental Fig. S9), suggesting that the fast movement of the vesicles is dependent on actin and myosin activity but the vesicles could still retain motility, possibly through free diffusion when actin or myosin activity is disrupted.

The increased number of cytoplasmic CESA compartments in myosin- and actin-deficient cells could result from exocytic vesicles whose secretion was disrupted, from increased internalization of CESAs through endocytosis, or both. To test whether endocytosis was altered in xi3KO and BDM-, PBP-, and LatB-treated cells, we utilized the lipophilic dye FM4-64, a marker for constitutive endocytosis (Dettmer et al., 2006; Sampathkumar et al., 2013), for an internalization assay in light-grown hypocotyl epidermal cells. The number of FM4-64-labeled endosomes was significantly reduced in the mutant and in cells pretreated with BDM, PBP, or LatB for 30 min (Supplemental Figure S10, A and C). These results were consistent with a previous study showing that endocytosis of FM4-64 was greatly inhibited in a myosin xi1 xi2 xii xik quadruple-knockout mutant (Yang et al., 2014).

BDM has also been shown to inhibit the ligand-induced endocytosis of the PM defense receptor FLAGELLIN SENSING2 (FLS2; Beck et al., 2012). We quantified the number of internalized FLS2 endosomes by pretreating an Arabidopsis FLS2-GFP transgenic line with BDM or PBP followed by elicitation with the flagellin-derived ligand flg22. Both BDM and PBP treatment greatly reduced the number of internalized FLS2 endosomes compared with mock treatment (Supplemental Figure S10, B and D). The internalization assays indicated that perturbation of myosin activity inhibited both constitutive and receptor-mediated endocytosis; therefore, the cortical CESA compartments that accumulated in myosin- and actin-deficient cells were more likely to be vesicles that were unable to deliver CESAs to the PM rather than newly internalized endosomes. These data support a role of cortical actin and myosin in mediating exocytic trafficking of CESA compartments for CSC delivery.

Because disruption of myosin activity alters actin organization and dynamics (Peremyslov et al., 2010; Ueda et al., 2010; Park and Nebenführ, 2013; Cai et al., 2014; Madison et al., 2015), we tested whether the accumulation of cortical CESA compartments in xi3KO and myosin inhibitor-treated cells resulted from perturbation of the actin cytoskeleton. We analyzed the density and extent of bundling of actin arrays in the cortical and subcortical cytoplasm, respectively. In wild-type cells, the density of actin filaments was significantly higher and less bundled in the cortex compared with that in the subcortex (Supplemental Fig. S11). In xi3KO and

BDM- and PBP-treated cells, a similar overall pattern of cortical and subcortical actin architecture was observed, although the average density was decreased and the extent of bundling was increased in the mutant and PBP-treated cells. By contrast, cells treated with BDM had the opposite phenotype with higher filament densities in both the cortex and subcortex and reduced extent of bundling, compared with wild-type cells (Supplemental Figure S11; Supplemental Table S2). These data indicate that the preferential accumulation of CESA compartments in the cortex in xi3KO or myosin inhibitor-treated cells is unlikely due to a specific alteration of actin architecture.

The SNARE protein SYP61 is a TGN/EE marker, and SYP61 compartments have been implicated in exocytic trafficking and transport of various cargoes, including CESA (Drakakaki et al., 2012). After treatment of etiolated hypocotyls expressing SYP61-CFP with BDM, PBP, and LatB, we detected a significant increase in the number of small SYP61 vesicles in the cell cortex, but not in the subcortex, compared with control cells (Supplemental Figure S12). These results reveal that actin and myosin are also involved in the trafficking of SYP61 vesicles and may play a role in general exocytic membrane trafficking.

Previous studies have shown that a population of CESA compartments colocalize with SYP61 (Gutierrez et al., 2009). To test whether the accumulated cortical CESA and SYP61 compartments in myosin- and actin-deficient cells are identical, we generated a line coexpressing YFP-CESA6 and SYP61-CFP and performed a colocalization assay. After BDM, PBP, and LatB treatment, the abundance of both YFP-only and CFP-only compartments increased significantly, whereas the population with overlapping signals remained constant (Fig. 6, A and B). In mock-treated cells, 33% of the cortical vesicles had both YFP and CFP signals; however, after inhibitor treatments, the percentage of vesicles with overlapping signals was reduced to 20% or less (Fig. 6C). These results demonstrate that cortical CESA and SYP61 compartments that accumulate following myosin inhibition are distinct populations that do not significantly overlap.

Myosin Disruption Results in CSC Secretion Failure at the PM

One possibility for the abnormal accumulation of motile CESA compartments near the PM in myosin- and actin-deficient cells is that their secretion was inhibited. To test whether myosin plays a role in vesicle exocytosis, we observed individual CSC insertion events at the PM in epidermal cells from the middle region of the hypocotyl, where CSC particles are less dense and visualization of individual particle insertion was possible (Crowell et al., 2009). For the high-resolution spatiotemporal CSC insertion assay, seedlings were mounted directly in mock or inhibitor solutions to minimize inhibitor treatment time, and time-lapse series
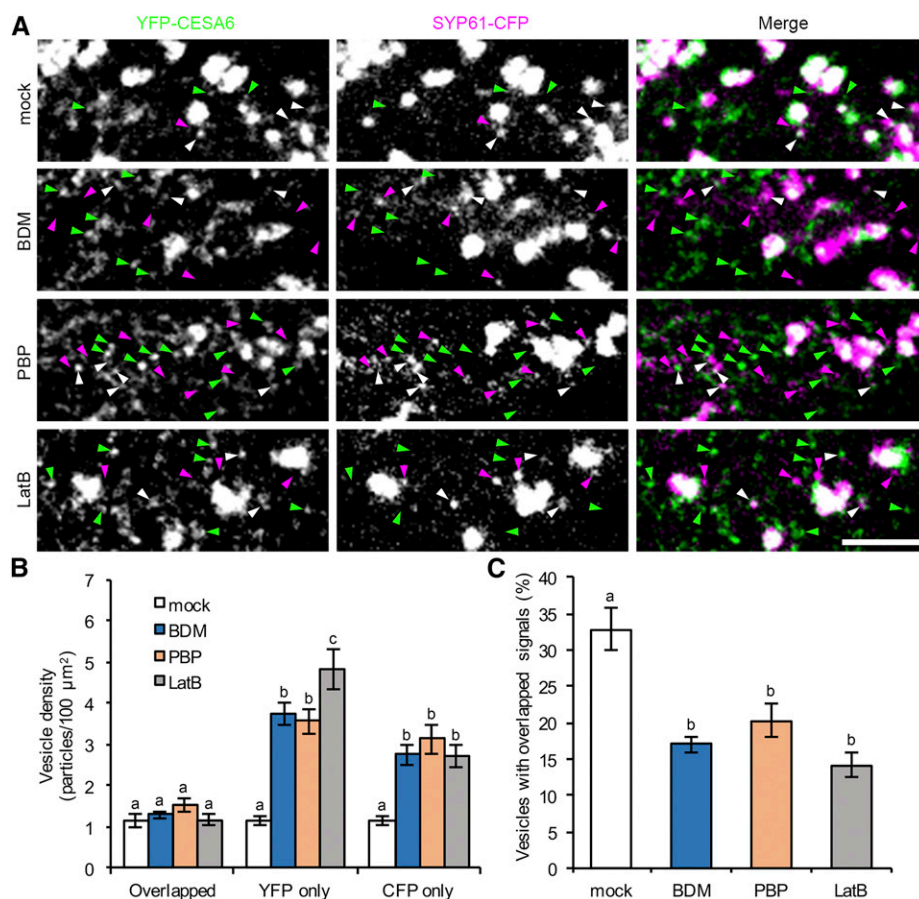
Figure 6. Myosin inhibitors cause an accumulation of distinct CESA6 and SYP61 compartments in the cortical cytoplasm. A, Representative single optical sections taken from the cortical cytoplasm in etiolated hypocotyl epidermal cells coexpressing YFP-CESA6 and SYP61-CFP. Seedlings were treated with inhibitors for 15 min prior to imaging. Vesicles labeled with YFP only, CFP only, or with both markers are indicated by green, magenta, and white arrowheads, respectively. Bar, 5 μm. B, Quantitative analysis of vesicle density shows that the number of YFP-only and CFP-only compartments was significantly increased after BDM, PBP, and LatB treatment; by contrast, the number of compartments with overlapping signals did not show major differences compared with mock-treated cells. C, The percentage of vesicles with overlapping signals decreased significantly in BDM-, PBP-, and LatB-treated cells. Values given are means $\pm$ SE ($n \geq 20$ cells from six seedlings for each treatment; a total of 263, 586, 529, and 578 compartments were measured from total areas of 7,804, 7,649, 6,339, and 6,880 μm^2 in mock and BDM-, PBP-, and LatB-treated cells, respectively; one-way ANOVA with Tukey's post-hoc test, letters [a–c] denote samples/groups that show statistically significant differences with other groups, $P < 0.05$).

were acquired at 3-s intervals for 12 min. Similar to a previous report (Gutierrez et al., 2009), we observed that a newly arrived CSC particle typically displayed three phases of movement: (1) a short erratic phase with rapid and local movements near the PM, (2) a static or pause phase for 1 to 2 min in a fixed location, and (3) a steady migration phase as active cellulose-producing complexes translocate in the plane of the PM (Fig. 7A; Supplemental Movie S4). We also observed that most of the CSC insertion sites were coincident with cortical microtubules (Supplemental Figure S13; Supplemental Movie S5), which was consistent with a previous report (Gutierrez et al., 2009).

The initial erratic phase of CSC particles is thought to represent the transient behavior of trafficking compartments before they dock and fuse to the destination

PM to deliver CSCs (Gutierrez et al., 2009). In this study, we observed a total of 564 insertion events, and 378 of them (67%) were associated with an erratically moving CESA compartment; these compartments often translocated in close association with Golgi, or were separate from a Golgi body, before they stabilized and paused at the PM (Fig. 7A; Supplemental Movies S4, S5, S6, and S7). The frequency of the erratic phase was similar to a previous report (37 out of 60; Gutierrez et al., 2009). In the remainder of the delivery events, either pausing of a CESA-containing Golgi was observed to coincide with a new insertion or no obvious delivery compartment/organelle was observed. Our results confirm that the cytoplasmic CESA vesicles are the major delivery compartments for CSC localization in the PM.
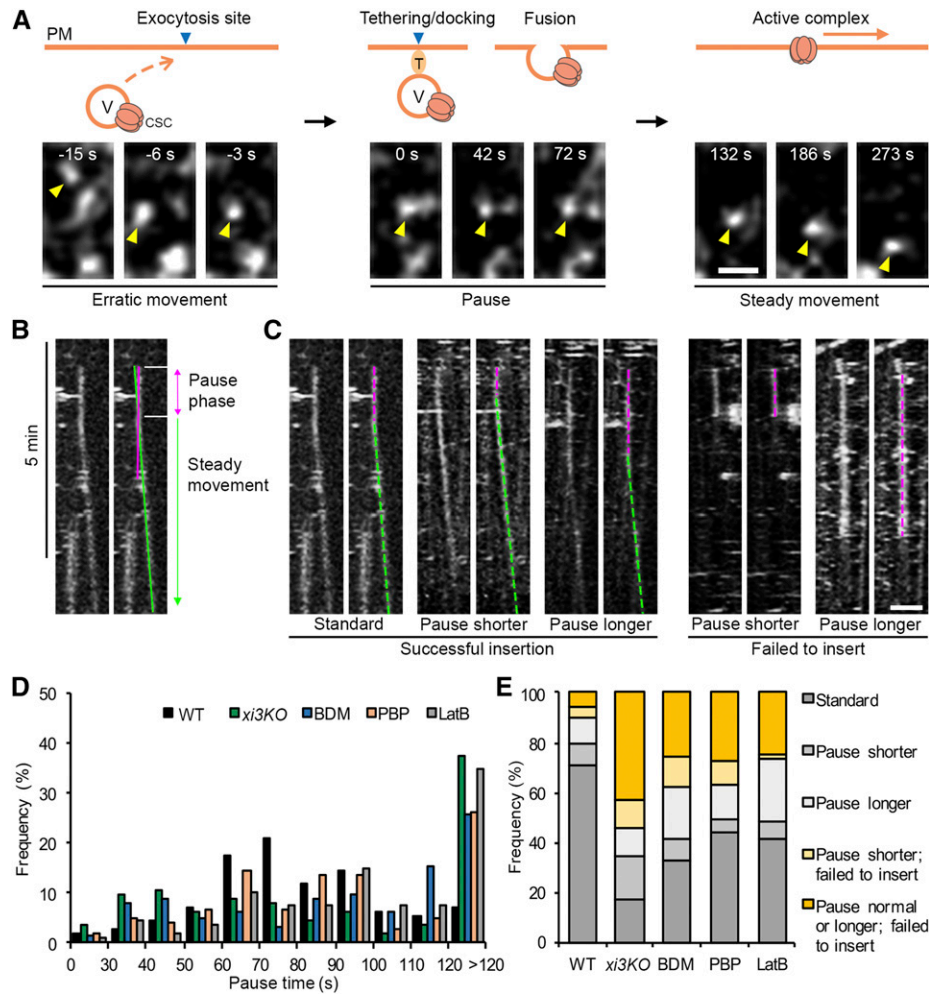
Figure 7. Inhibition of myosin causes CSC insertion failures at the PM. A, Representative images show a typical CSC insertion event at the PM. A CESA particle (yellow arrowhead) arriving in the cortex initially undergoes erratic motility, which likely represents a delivery vesicle (V) that is transported to an exocytosis site. The particle then pauses (marked as 0 s) and exhibits a static phase for ~80 s in a fixed position, which likely corresponds to tethering, docking, and fusion of the delivery compartment to the PM. After the CSC particle is inserted, it shows steady movement at the PM as an active complex. T, Tethering proteins. Bar, 1 μm. B, Representative kymograph of the CSC insertion event shown in A illustrates the pause phase and the steady movement phase. The exact duration of the pause phase was determined by fitting a straight line (green) along the moving trajectory and another line (magenta) along the pause phase. The intersection of the two lines was defined as the end of the pause phase. C, Representative kymographs show five categories of insertion events from left to right: standard insertion with normal pause time, insertion that has a shorter pause time, insertion that has a longer pause time, a shorter pause time and failure to insert, and a longer pause time and failure to insert. Pause phases are marked with magenta dashed lines, and steady movement phases are marked with green dashed lines. Bar, 2 μm. D, Distribution of particle pause times ($n \geq 11$ cells from seven seedlings for each genotype or treatment; a total of 114, 113, 124, 104, and 109 events were measured in wild type [WT], *xi3KO*, and BDM-, PBP-, and LatB-treated cells, respectively). E, The proportion of five types of insertion events described in C in wild-type, *xi3KO*, and BDM-, PBP-, and LatB-treated cells. A shorter or longer pause time was defined as the mean value (81 $\pm$ 27 s) of particle pause time in wild type minus (<54 s) or plus 1 SD (>108 s), respectively.

The exocyst complex and an exocytosis-related protein PATROL1 were shown to colocalize with CSCs during the first few seconds of the pause phase (Zhu et al., 2018), suggesting that pausing is a necessary step related to vesicle tethering and fusion for CSC delivery to the PM. Thus, measuring the duration of the pause phase represents a way to assess the secretion process of CSCs. In this assay, only particles that showed de novo appearance at the PM plane followed by a static phase for more than 5 frames (>15 s) were tracked and considered as insertion or attempted insertion events. By tracking the newly inserted particles over time, we found that the insertion events mainly fell into the following categories: (1) particles that paused for 1 to 2 min followed by steady movement as an active CSC complex (Fig. 7C, Supplemental Movie S4); (2) particles that paused for a significantly shorter or longer time, followed by steady migration as an active CSC complex

(Fig. 7C); and (3) particles that underwent a pause phase but then disappeared or rapidly moved away, so no CSC was inserted, representing a failed insertion/secretion event (Fig. 7C; Supplemental Movies S6 and S7). We quantified each type of event and measured particle pause time by analysis of kymographs (Fig. 7B). In the wild type, the average CSC pause time was 81 ± 27 s (n = 110 events), which was close to the previously reported value (62 ± 23 s; Gutierrez et al., 2009). Notably, particle pause time was greatly altered in *xi3KO* or inhibitor-treated cells (Fig. 7D). To define aberrant pausing, we used the mean value of particle pause time in the wild type minus or plus 1 sd; thus, pause times < 54 s or > 108 s were considered as shorter or longer pause events, respectively. We found that in *xi3KO* or inhibitor-treated cells, more than 30% of the insertions exhibited a longer pause time (>108 s); moreover, there was a slightly increased population that paused only for 30 to 50 s in *xi3KO* and BDM- and PBP-treated cells (Fig. 7D). Overall, the percentage of failed insertion events increased by 2- to 5-fold in the mutant or inhibitor-treated cells compared with the wild type (Fig. 7E). In the wild type, only 10% of the observed events failed to deliver a functional CSC (11 of 114 events); however, in *xi3KO*, the proportion increased to 55% (62 of 113 events), and upon BDM, PBP, and LatB treatment, it increased to 37% (46 of 124 events), 37% (38 of 104 events), and 26% (28 of 109 events), respectively (Fig. 7E). The abnormal CSC pause time and increased insertion failures at the PM indicate that cortical actin and myosin activity are required for exocytosis of CESA compartments, probably through mediating vesicle tethering or fusion to the PM.

Cortical microtubules have been shown to define the CSC insertion sites, and CESA compartments are tethered to microtubules through CELLULOSE SYNTHASE INTERACTIVE1 for CSC delivery (Gutierrez et al., 2009; Bringmann et al., 2012; Zhu et al., 2018). Another report showed that the frequency of microtubule-localized insertion of CSCs is not affected in LatB-treated cells or in the *act2 act7* double mutant (Sampathkumar et al., 2013). We tested whether disruption of myosin might affect the preferential insertion of CSCs next to microtubules, and our results showed that after treatment with BDM, PBP, or LatB, most of the CSC insertion events (~85%) observed were still coincident with microtubules, at a frequency similar to that in untreated cells (Supplemental Fig. S13). Therefore, myosin and actin activity are not necessary for CSCs to reach the cortical microtubule sites but are required for the later stages of vesicle tethering and fusion to the PM.

MYOSIN XIK Associates Transiently with CSCs during Vesicle Tethering

To test whether myosin motors participate directly in CSC secretion at the PM, we performed a colocalization assay by coexpressing XIK-YFP driven by its native promoter (Peremyslov et al., 2012) and tdTomato-CESA6 (Sampathkumar et al., 2013) in the *prc1-1* homozygous mutant background. In hypocotyl epidermal cells, the XIK-YFP signal comprises small dense compartments that move rapidly along F-actin, with a minor fraction as scattered patches in the cortical cytoplasm as shown previously (Peremyslov et al., 2012; Supplemental Movie S8). To determine the spatiotemporal localization of XIK-YFP and tdTomato-CESA6 during CSC insertion, we acquired two-color time-lapse series and analyzed individual CSC insertion events at the PM. In most cases, we observed a patch or cluster of diffuse XIK-YFP fluorescence that arrived with a CSC particle or vesicle in the vicinity of the PM and remained during the first few seconds after the particle paused at the PM (82 out of 86 events; Fig. 8, A and B; Supplemental Movie S8). These cytoplasmic XIK-YFP patches were highly irregular and dynamic and were distinct from the brighter XIK-YFP-labeled vesicle clusters that travel in linear paths along F-actin (Supplemental Movie S8). One explanation for the diffuse pattern of XIK-YFP fluorescence could be that MYOSIN XIK is associated with vesicle clusters rather than distinct CESA compartments. It has been shown that secretory vesicles in plants are transported to the PM as clusters (Toyooka et al., 2009).

To confirm that the XIK-YFP fluorescence patches were specifically associated with CSC insertion rather than some random events, we performed quantitative analysis by tracking individual CSC insertion events from the erratic phase to the pause phase and steady migration phase and measured the fluorescence intensity in the XIK-YFP channel in a small region of interest (ROI) that overlapped with the tdTomato-CESA6 signal (Fig. 8C; Supplemental Fig. S14). The average fluorescence intensity of XIK-YFP in the ROI was significantly higher during the erratic phase, and the first 3 s of the pause phase compared with the remainder of the pause phase or active translocation in the plane of the PM (Fig. 8D). These data demonstrate that XIK-YFP is specifically associated with the arrival and the initial pause or tethering phase of a CSC particle, thereby supporting a direct role for myosin in exocytosis of CESA compartments at the PM.

DISCUSSION

In plants, a cortical actin-myosin cytoskeletal network regulates cytoplasmic streaming and long-distance transport of diverse intracellular organelles and vesicles. It also promotes cell expansion and growth. However, it remains unclear whether actin and myosin also direct vesicle exocytosis and protein secretion at the PM. In this study, by investigating the trafficking of CSC complexes, we demonstrate a previously undiscovered role for myosin XI in post-Golgi vesicle trafficking and cell wall synthesis. The large size of individual CSC particles as well as their organized
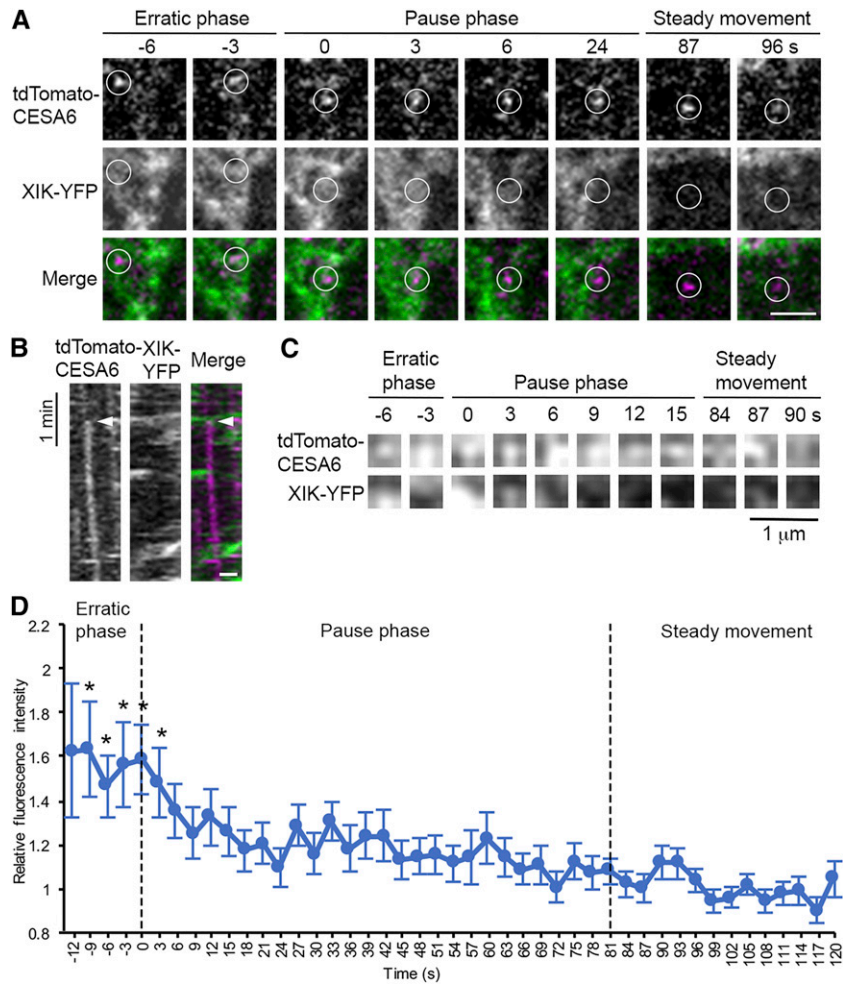
Figure 8. Arrival of MYOSIN XIK at the site of CESA6 insertion into the PM is early and transient. MYOSIN XIK-YFP and tdTomato-CESA6 were visualized at insertion sites by two-color time-lapse imaging using SDCM. A, Representative images from a time series taken from the cortical cytoplasm of a hypocotyl epidermal cell show that diffuse XIK-YFP signal was colocalized with a newly arrived CSC vesicle (white circles) during the entirety of the erratic phase as well as the first few seconds of the pause phase, but not during the steady migration phase. In the merged images, the XIK-YFP channel is shown in green and tdTomato-CESA6 in magenta. The entire time series is available as Supplemental Movie S8. Bar, 2 μm. B, Kymograph prepared from representative images shown in A demonstrates transient colocalization of XIK-YFP (green) with tdTomato-CESA6 (magenta) at the beginning of the pause phase (white arrowheads). Bar, 1 μm. C, Another representative time-lapse series showing a small ROI (3 × 3 pixels) selected at the centroid of a single CSC vesicle or particle. The ROI, defined by the presence of CESA6, was tracked in both channels during the erratic phase, pause phase, and the steady movement phase. The ROI in the XIK-YFP channel was extracted for analysis of fluorescence intensity. D, Quantitative analysis of mean fluorescence intensity of XIK-YFP in ROIs from multiple insertion events in different epidermal cells. The fluorescence intensity was normalized using the intensity of the ROI in each frame divided by the average intensity of ROIs from the steady movement phase, assuming that any myosin associated with an active translocating CSC represents a random event. There was significantly higher fluorescence intensity of XIK-YFP during the erratic phase of CSC particles as well as the first 3 s of the pause phase, compared with the remainder of the pause phase and the beginning of the steady movement phase. Values given are means ± SE (n = 64 insertion events analyzed from 13 cells in seven seedlings; because the duration of the erratic phase varied among different insertion events, the sample sizes at −12 s, −9 s, −6 s, and −3 s were 5, 16, 28, and 50, respectively; X-bar and S Control Charts were used for statistical comparison of timepoints; *$P < 0.05$).

spatial distribution and motility pattern at the PM enable the visualization of individual vesicle secretion events and make them an excellent cargo for studying exocytosis in plants. We observed that in cells with reduced myosin or actin activity, many CESA delivery compartments exhibited prolonged pausing at the PM and/or failure to deliver a functional CSC into the PM. In addition, we detected a marked increase in the retention or accumulation of small CESA compartments in the cortical cytoplasm, which likely results from failed insertion events. The secretion defects correlated with a reduced overall delivery rate and decreased

density of CSCs at the PM. Moreover, colocalization of MYOSIN XIK with cortical CESA compartments and the presence of XIK at CSC insertion sites suggest that the role of myosin in post-Golgi vesicle trafficking is likely through direct interaction with vesicle cargo. These new findings reveal a specific role for actin and myosin in vesicle exocytosis, possibly by regulating vesicle tethering or fusion (Fig. 9).

In animal and fungal cells, myosin motors have well-established roles in secretory vesicle trafficking. They not only transport vesicles to their secretion sites, but also participate in the subsequent exocytosis process. Yeast myosin V, Myo2p, has been shown to regulate tethering of secretory vesicles to the PM before fusion, and the tethering time is significantly extended in a *myo2p* mutant (Donovan and Bretscher, 2015). In hippocampal neurons, myosin V also plays a role in synaptic vesicle tethering at the PM to regulate neurotransmitter release (Maschi et al., 2018). In our high-resolution secretion assays, we observed an increased frequency of CESA vesicles that paused longer at the PM in both the *xi3KO* mutant and upon acute myosin inhibitor treatment. Similar results were observed following LatB treatment. It seems likely that myosin XI and actin regulate the tethering of CESA vesicles at the PM, although the detailed mechanism remains to be elucidated. In addition, yeast Myo2p interacts directly with the Sec15 subunit of the exocyst tethering complex, and disruption of this interaction blocks secretion and causes significant accumulation of secretory vesicles within the cell (Jin et al., 2011). Considering that the cargo-binding domains of myosins XI are homologous to those of myosin V (Sattarzadeh et al., 2013), and the exocyst shares highly conserved subunit composition and biological functions across eukaryotes (Hála et al., 2008; Synek et al., 2014), plant myosins XI are likely to have conserved function through interaction with exocyst components to regulate vesicle exocytosis. There is limited evidence in plant cells suggesting the interaction of myosin with tethering components; for example, Arabidopsis MYOSIN XIK cofractionated with the exocyst marker Sec6 in root extracts (Peremyslov et al., 2012). The actin cytoskeleton cooperates with the exocyst subunit EXO84B to execute post-Golgi trafficking of

the ATP-binding cassette transporter PENETRATION3 to the outer periclinal membrane of root epidermal cells (Mao et al., 2016); however, myosin involvement in this polar trafficking has not yet been established.

Our finding of increased number of cortical vesicles in the *xi3KO* mutant or inhibitor-treated cells further supports the hypothesis that myosin XI is involved in vesicle tethering. In plants, the phenotype of accumulation of cortical vesicles is a typical feature found in mutants that are deficient in vesicle tethering. For example, mutations in the exocyst tethering complex, *exo84b*, and the TRAPPII tethering complex, *trs120* and *trs130*, show abnormal accumulation of vesicles in the cortical cytoplasm in Arabidopsis (Fendrych et al., 2010; Qi et al., 2011). Exocyst subunits have been implicated in both primary and secondary cell wall deposition in Arabidopsis (Vukašinović et al., 2017; Zhu et al., 2018). Although we cannot rule out the possibility that some of the accumulated compartments in myosin- or actin-deficient cells resulted from endocytosis or endocytic vesicles whose intracellular trafficking was interrupted, our studies on internalization of FM4-64 and FLS2 suggest that endocytosis is inhibited in cells with reduced actin and/or myosin activity. In addition, another study shows that following 10-min treatment with mannitol, which increases the number of cortical CESA compartments, the FM4-64 endosomes did not coincide with the CESA compartments, indicating that these vesicles are unlikely to be newly internalized compartments (Gutierrez et al., 2009). Combining the observations of high frequency of vesicle secretion failure and reduced CSC delivery rate in myosin-inhibited cells, we believe that a majority of the accumulated CESA compartments are secretory vesicles, and their accumulation is due to failed membrane tethering and fusion. An overlapping possibility for their accumulation could be that if these are secretory vesicles that failed to fuse to the PM, they might lack the machinery to be transported away from the cortex for recycling or degradation that is associated with newly formed endocytic vesicles.

A cortical vesicle accumulation phenotype has also been characterized in plant cytokinesis-defective mutants with impaired membrane trafficking during cell
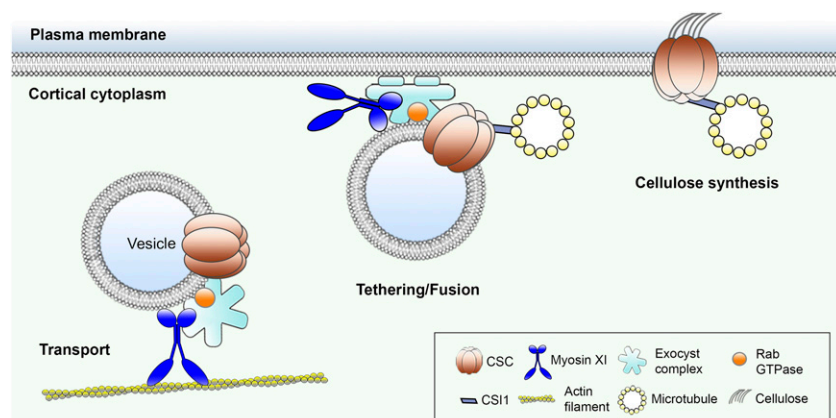

Figure 9. Myosin plays a novel role in vesicle tethering or fusion. This illustration portrays the known and hypothetical roles of myosin XI in delivery of CSCs to the plasma membrane. Based on evidence presented here, as well as recent publications, we predict that myosin not only transports CESA-containing vesicles in the cell cortex, but also participates in vesicle tethering or fusion after vesicles reach the CSC insertion sites that are defined by CELLULOSE SYNTHASE INTERACTIVE1 (CSI1) and microtubules. The potential role of myosin in exocytosis could be through interaction with the exocyst complex to stabilize or maintain an intact tethering complex required for fusion with the membrane.

plate formation, such as mutations in *KNOLLE* and *KEULE* encoding syntaxins or syntaxin regulatory proteins that are required for membrane fusion (Lauber et al., 1997; Waizenegger et al., 2000). Mutations of *STOMATAL CYTOKINESIS DEFECTIVE1* (*SCD1*) exhibit secretory vesicle accumulation in cytokinesis-defective cells as well as perturbed cell plate formation. SCD1 and SCD2 have been shown to regulate post-Golgi vesicle exocytosis to the PM through interaction with RabE1 and the exocyst complex (Falbel et al., 2003; Mayers et al., 2017). A recent study also shows concentration of MYOSIN XIK at the forming cell plate in root and shoot meristem cells, and the *xi3KO* mutant displays defects in cell division plane alignment (Abu-Abied et al., 2018). Although it remains unclear how myosins XI are involved in cell plate formation and cytokinesis, our findings that myosins XI play a role in exocytic trafficking provides clues that the class XI myosins may share similar functions by mediating secretory membrane trafficking and/or homotypic vesicle fusion during cell plate formation. Further study is required to define and characterize molecular interactions between actin cytoskeletal components and vesicle-trafficking machinery proteins, like the exocyst complex or Rab proteins, in the cortical cytoplasm of plant cells. The new role of myosin XI in exocytosis and protein secretion advances our understanding of how myosin activity is correlated with plant cell growth and could help explain the previously described phenotypes in *myosin xi* mutants, such as reduced cell expansion/elongation rate, polar auxin transport, and plant size (Peremyslov et al., 2010; Ojangu et al., 2012; Madison et al., 2015; Ueda et al., 2015; Abu-Abied et al., 2018; Ryan and Nebenführ, 2018).

Our colocalization studies reveal that cortical CESA compartments that accumulate in myosin- or actin-deficient cells are distinct from SYP61 or TGN-related compartments, which also accumulate upon myosin inhibition. Some previous studies indicate that the plant TGN/EEs are involved in both endocytic and secretory trafficking; SYP61 vesicles derived from the TGN are thought to mediate the delivery of various cargos to the PM (Viotti et al., 2010; Drakakaki et al., 2012). Perturbation of V-ATPase function in the TGN/EE has been shown to affect the exocytic trafficking of CESAs (Luo et al., 2015). However, another study showed that CESA compartments that colabeled with the TGN/EE marker V-type proton ATPase subunit a1-mRFP did not associate with CSC insertion at the PM and are thought to be mainly endocytic compartments (Crowell et al., 2009). Similarly, our results indicate that CESAs are delivered by compartments that do not overlap with SYP61-associated vesicles, which again challenges the role of TGN/EEs in de novo secretion of CSCs at the PM. An alternative explanation is that CESA proteins pass through TGN/EEs at an early stage but are later packaged into a unique compartment for delivery and due to inhibition of secretion upon myosin disruption are trapped in the cortical cytoplasm.

Since the primary role of the plant actin-myosin transport network is to power cytoplasmic streaming and intracellular organelle motility, it is possible that the cellulose synthesis and trafficking defects detected in myosin- or actin-deficient cells were mainly due to a general perturbation of organelle and vesicle motility. However, our results suggest that this is unlikely the case. We show that in the *xi3KO* mutant that is known to have severely impaired Golgi motility and cytoplasmic streaming rate (Prokhnevsky et al., 2008; Peremyslov et al., 2010), a large motile population of cortical vesicles close to the PM could be detected, and they subsequently paused at the PM for CSC delivery, although many of them failed to deliver a CSC particle. This suggests that even though these vesicles rely on the actin cytoskeleton for long-distance transport, their relatively short and local movement to the PM does not necessarily require actin tracks. Similarly, previous reports show that LatB treatment causes gross clustering of Golgi and that CSCs are delivered only to the nearby region (Gutierrez et al., 2009; Sampathkumar et al., 2013), suggesting that the delivery compartments can still travel a certain distance in the cortex but not too far away from Golgi when the cortical actin network is disrupted. In addition, we showed that in the *xi3KO* mutant and upon acute myosin inhibitor treatment, the global Golgi distribution was not greatly affected and no apparent Golgi clustering was detected. Therefore, the CSC trafficking defects in those cells were unlikely caused by a lack of transport of delivery compartments to the PM, but due to inhibition of exocytosis at the PM.

Unexpectedly, we found that myosin perturbation affects the velocity of CSC translocation in the plane of the PM. Because steady movement of CSCs is thought to be powered by the enzymatic activity of CESAs (Paredez et al., 2006; Diotallevi and Mulder, 2007; Wallace and Somerville, 2015), the role of myosin XI is likely to be indirect. One hypothesis is that inhibition of endocytosis in myosin-deficient cells increases the number of slower-moving faulty CSCs compared to fully functional CSCs. Similar inhibition of CSC velocities is detected in the Arabidopsis *twd40-2* or *ap2m twd40-2* double mutants and in plants with constitutive silencing of the TPLATE complex; these proteins are components of the clathrin-mediated endocytosis pathway and are involved in CSC internalization (Bashline et al., 2015; Sánchez-Rodríguez et al., 2018). Conversely, a delay or incomplete vesicle fusion, like that postulated for exocyst complex mutants (e.g. *sec5*), could cause the accumulation of faulty CSCs held in proximity to the PM (Zhu et al., 2018). It should be noted that in contrast to genetic or chemical perturbation of myosin, treatment of cells with LatB had only a modest or no effect on CSC motility in the plane of PM (Supplemental Table S2), as previously reported for actin disruptions (Sampathkumar et al., 2013). This indicates that although the role of myosin as a molecular motor is largely dependent on the actin cytoskeleton, myosin could have a specific role independent of actin. In addition, we observed that myosin inhibitor

treatment, but not LatB, rapidly decreased CESA density at the PM. Similar to a previous publication (Beck et al., 2012), we found that internalization of FLS2 through receptor-mediated endocytosis was markedly reduced with PBP and BDM treatment, but not by LatB. Collectively, these findings suggest that myosin may have a more critical role than actin in exocytic or endocytic trafficking. Determining the myosin-centric function in trafficking requires further investigation but could relate to vesicle fusion/scission at the PM.

MATERIALS AND METHODS

Plant Materials and Growth Conditions

An Arabidopsis (*Arabidopsis thaliana*) mutant with *myosin xi1*, *xi2*, and *xik* knocked out (*xi3KO*) and the *xi3KO* mutant expressing venusYFP-fABD2 were characterized previously (Peremyslov et al., 2010; Cai et al., 2014). Homozygous YFP-CESA6 *prc1-1* seeds were generated previously (Paredez et al., 2006; Li et al., 2012) and kindly provided by Ying Gu (Penn State University). The *xi3KO* mutant was crossed to YFP-CESA6 *prc1-1*, and F2 homozygous mutants and wild-type siblings in the presence of *prc1-1* were recovered. For the XIK-YFP lines, a construct carrying a genomic copy of the *MYOSIN XIK* gene tagged with YFP previously described by Peremyslov et al. (2012) was transformed into *xi3KO* mutant plants, or plants expressing tdTomato-CESA6 (Sampathkumar et al., 2013), by *Agrobacterium*-mediated transformation through floral dip (Zhang et al., 2006). For the YFP-CESA6 and SYP61-CFP double-marked line, YFP-CESA6 plants were crossed with plants expressing SYP61-CFP, and F1 plants were used for imaging. Transgenic lines of YFP-TUB5 (Shaw et al., 2003), FLS2-GFP (Beck et al., 2012), PIN2-GFP (Xu and Scheres, 2005), BRI1-GFP (Geldner et al., 2007), and SYP61-CFP (Robert et al., 2008) were described previously. Seeds of plants expressing YFP-Mannosidase I were ordered from the Arabidopsis Biological Resource Center (Ohio State University). The YFP-CESA6 mCherry-TUA5 coexpression line was kindly provided by David W. Ehrhardt (Carnegie Institution for Science).

The Arabidopsis seeds were surface sterilized and stratified at 4°C for 3 d on half-strength Murashige and Skoog medium supplemented with 1% Suc and 0.8% agar. For light growth, plants were grown under long-day lighting conditions (16 h light/8 h dark) at 21°C. For dark growth, plates were exposed to light for 4 h and then placed vertically and kept at 21°C for 3 d in continuous darkness.

Drug Treatment

For cellulose content and monosaccharide composition analysis, wild-type seedlings were grown on half-strength Murashige and Skoog plates containing 100 nM LatB (Sigma-Aldrich) or 3 mM BDM (Sigma-Aldrich) for 5 d. For short-term live-cell treatments, seedlings were presoaked in drug solutions in 24-well plates in the dark. For CSC delivery assays using FRAP and CSC insertion assays, hypocotyls were mounted in inhibitor solutions and imaged immediately. LatB, PBP (Adipogen), and MyoVin-1 (EMD Millipore) were dissolved in DMSO to prepare a 5-mM stock solution. BDM was dissolved in water immediately before use. For propidium iodide (PI) staining, seedlings were presoaked for 30 s in 10 μg mL^{-1} PI solution dissolved in water. FM4-64 was dissolved in DMSO and used at a concentration of 20 μM.

Live-Cell Imaging

For image acquisition, epidermal cells at the apical region of 3-d-old dark-grown hypocotyls were used unless otherwise stated. For excitation of YFP-CESA6, XIK-YFP, YFP-TUB5, vYFP-fABD2, secGFP, and SYP61-CFP, SDCM was performed using a Yokogawa CSU-X1-A1 scanner unit mounted on an Olympus IX-83 microscope, equipped with a 100× 1.45-numerical aperture (NA) UPlanSApo oil objective (Olympus) and an Andor iXon Ultra 897BV EMCCD camera (Andor Technology). YFP, GFP, CFP, and mCherry/tdTomato fluorescence were excited with 514-nm, 488-nm, 445-nm, and 561-nm laser lines and emission collected through 542/27-nm, 525/30-nm, 479/40-nm, and 607/36-nm filters, respectively. For YFP-Mannosidase I imaging, variable-angle

epifluorescence microscopy was performed using a TIRF illuminator on an IX-71 microscope (Olympus) as described by Cai et al. (2014). For CSC density and motility imaging, time-lapse images were collected at the PM with a 5-s interval for 5 or 61 frames, respectively. For cortical and subcortical YFP-CESA6 and SYP61-CFP imaging, z-series at 0.2-μm step sizes plus time lapse with 1.6-s intervals for 35 frames were collected. For cortical and subcortical actin analysis, propidium iodide was used to label the cell wall and as an indicator of the PM plane. Dual-wavelength imaging was performed, and z-series at 0.2-μm step sizes were collected. For dual-wavelength imaging of YFP-CESA6 mCherry-TUA5 and XIK-YFP tdTomato-CESA6, time-lapse images were collected at the PM focal plane with 3-s intervals for 10 or 12 min. For all dual-wavelength image acquisition, single-marked lines were tested initially to make sure there was no bleed-through in each channel. PIN2-GFP and BRI1-GFP were imaged in 6-d-old light-grown roots by SDCM as described above with a 60× 1.42 NA UPlanSApo oil objective (Olympus).

For FRAP experiments, images were collected with a Zeiss Observer Z.1 microscope, equipped with a Yokogawa CSU-X1 and a 100× 1.46 NA PlanApo objective (Zeiss). Photobleaching was performed with a Vector scanner (Intelligent Imaging Innovations) with a 515-nm laser line at 100% power and 3 ms/scan. Time-lapse images were collected at the PM with a 10-s interval for 76 frames, with photobleaching in a small region (44.2 μm^2) after the third frame, and recovery monitored for a total of 12 min.

Image Processing and Quantitative Analysis

Image processing and analysis were performed with ImageJ and FIJI (Schindelin et al., 2012). Image drift was corrected with the StackReg plug-in. Golgi motility was analyzed with the TrackMate plug-in and a Laplacian of Gaussian algorithm as the particle detection filter. Trajectories detected by TrackMate were selected for analysis only if more than five spots were on the trajectory. The parameter "Mean Speed" was then pooled and plotted as the average Golgi motility rate. XIK-YFP motility was measured by the Multi Kymograph plug-in. For PM-localized CSC density analysis, the first frames of time-lapse images were used and no intensity adjustment was made. The number of CSCs was then counted by the TrackMate plug-in with Difference of Gaussians algorithm. CSC density was calculated as the number of particles detected divided by the area of the analyzed region. For PM-localized CSC motility assays, average intensity projections were generated with the time-lapse series to identify the trajectories of the CSC particles over time. Kymographs were generated by following the trajectories of CSC particles, and CSC motility rate was calculated as the reciprocal of the slope of individual CSC particles in kymographs.

For FRAP assays, a smaller area (28.3 μm^2) within the bleached region was used for analysis to exclude the lateral movement of CSCs into the bleached region (Sampathkumar et al., 2013). The newly delivered CSCs during the initial 5 min of recovery were manually counted, and the criteria used to define a CSC delivery event were as described previously (Gutierrez et al., 2009; Li et al., 2016). Only the newly inserted particles that exhibited a static phase followed by steady linear migration at the PM were counted as new delivery events. The CSC delivery rate was calculated as the number of delivery events divided by the measured area and time.

For cortical and subcortical vesicle assays, z-series taken at 0.2 μm and 0.4 μm below the PM were used for cortical cytoplasm analysis and focal planes from 0.6 μm to 1.0 μm as the subcortical cytoplasm. Image background was subtracted using the Subtract Background tool in FIJI with rolling ball radius set at 30 pixels. The number of CESA and SYP61 vesicles was counted manually based on their size (smaller than a Golgi or TGN compartment) and dynamic behavior in the time-lapse series (Gutierrez et al., 2009). To determine overlap between CESA and SYP61 vesicles, only signals from both fluorescence channels that moved in the same trajectory over time were scored as colocalization. Vesicle density was calculated as the number of particles detected divided by the area of the analyzed region. The velocities of CESA compartments were measured by semiautomatic tracking with MTrackJ (Meijering et al., 2012) or the Multi Kymograph plug-in. The mean velocity of each individual trajectories was used for data analysis.

For high-resolution spatiotemporal analysis of individual CSC insertion events, only particles that showed de novo appearance at the PM plane followed by a static or pause phase for more than five frames (>15 s) were considered as new insertion events. The pause phase was determined by analysis of kymographs. Only a straight line in the kymograph was considered as a pause event. The exact duration of particle pause time was determined by fitting a straight line along the moving trajectory and another line along the pause phase

on the kymograph. The intersection of the two lines was defined as the end of the pause phase. For analysis of colocalization between XIK-YFP and tdTomato-CESA6, time-lapse series at 3-s intervals were acquired by SDCM in both fluorescence channels, and individual CSC insertion events at the PM plane were tracked over time. Only successful insertion events showing both a pause and steady migration phase were analyzed. CSCs inserted by Golgi pausing were excluded in the quantitative assay to avoid any nonspecific XIK-YFP signal contributed by the pausing Golgi. For quantitative analysis, an ROI of 3 × 3 pixels (0.16 μm^2) at the centroid of the CSC particle was selected, and the particle was tracked during its arrival at the PM and erratic phase, throughout the pause phase, and during the steady movement phase (a total of 120 s after insertion). The beginning of the pause phase was defined as 0 s and was determined as the first time point of the straight vertical line in the kymograph with no pixel shift. The same ROI in the corresponding XIK-YFP channel was measured for mean fluorescence intensity at every time point. To remove background fluorescence, the mean fluorescence intensity of XIK-YFP in the ROI was subtracted from the mean background fluorescence intensity in each individual frame. The mean background fluorescence of each frame was measured by selecting an empty region out of the sample area. For normalization, the relative fluorescence intensity was calculated as the fluorescence intensity of the ROI in each frame divided by the average fluorescence intensity of ROIs from the steady migration phase, assuming that any myosin association with an active translocating CSC represents a random event.

The fluorescence of PIN2-GFP and BRI1-GFP was quantified in FIJI by selecting regions at the PM in 10 to 20 different cells in each root and mean fluorescence intensity from each ROI measured. For quantification of the cytosolic secGFP fluorescence, the mean fluorescence intensity in the cytosol was measured on maximum intensity projection images acquired with SDCM from 3-d-old etiolated hypocotyl epidermal cells. For normalization, the relative fluorescence intensity was calculated by dividing the average fluorescence intensity of each treatment by that of the mock treatment.

For analysis of actin filament array organization, actin filament density and the extent of bundling (skewness) were determined as described previously (Higaki et al., 2010; Henty et al., 2011).

FM4-64 Internalization Assay

Four-day-old light-grown seedlings of the wild type and the *xi3KO* mutant were presoaked in inhibitor solutions for 30 min followed by incubation in 20 μM FM4-64 plus the inhibitor solutions for 6 min in the dark. Images were collected at the hypocotyl epidermis with SDCM as described above with a 60× 1.42 NA UPlanSApo oil objective (Olympus). The number of internalized FM4-64 endosomes in individual cells was counted, and the density was calculated as the number of endosomes per 100 μm^2.

FLS2-GFP Internalization Assay

Seven-day-old transgenic seedlings expressing FLS2-GFP were presoaked in dH$_2$O overnight in continuous light to reduce wounding response as described previously (Smith et al., 2014). Seedlings were then soaked in inhibitor solutions for 30 min followed by treatment with 1 μM flg22 (NeoBioSci) plus the inhibitors for another 45 min to induce the endocytosis of FLS2. Cotyledon epidermal cells at the adaxial side were imaged by SDCM as described above with a 60× 1.42 NA UPlanSApo oil objective (Olympus). z-series were collected at a 0.5-μm step size for 21 frames. Maximum intensity projections were generated from the z-series, and quantitative analysis of internalized FLS2-GFP endosomes was done using the Advanced Weka Segmentation plug-in in FIJI as described by Smith et al. (2014).

Cytoplasmic Streaming Assay of *Chara corallina*

Young internodal cells of *C. corallina* less than 30 mm long were cut into ~7-mm pieces and soaked in the original culture water containing drugs in 24-well plates at room temperature. Light microscopy was performed using a Nikon E600 microscope with a 20× 0.5 NA Plan Fluor objective. Time-lapse images at 0.22-s intervals were collected with a CCD camera (ORCA-ER C4742-95; Hamamatsu Photonics) and Metamorph software (version 4.6r9). The velocity of individual particles was analyzed by manual tracking with the MTrackJ plug-in in FIJI. The mean velocities measured by the plug-in were pooled and used for statistical analysis.

Cell Wall Determination

Five-day-old dark-grown hypocotyls were lyophilized and ground in sodium dodecyl sulfate (SDS) buffer (1% SDS, 50 mM Tris-HCl, pH 7.2). The homogenate was washed sequentially with SDS buffer and 50% ethanol at 60°C, and washed with acetone at room temperature. The acetone was discarded and samples were vacuum dried overnight. The dry residue was defined as cell wall material (CWM).

The cellulose content was determined as modified from Updegraff (1969). In brief, about 2 to 3 mg of CWM was hydrolyzed with AN reagent (acetic acid:nitric acid:water = 8:1:2) at 100°C for 60 min; the insoluble material was collected after centrifugation at 2500g for 5 min and washed with water. Alternatively, about 2.5 mg of CWM was hydrolyzed in 2 M TFA containing 500 nmol mL^{-1} of *myo*-inositol (internal standard) at 120°C for 90 min. The insoluble material was collected by centrifugation as above, and the soluble fraction saved for noncellulosic monosaccharide analysis. The amounts of sugar in the insoluble fractions from both the AN and TFA hydrolysis were measured using phenol-sulfuric colorimetric assay compared to cellulose standards (Dubois et al., 1956).

Noncellulosic monosaccharide composition in the supernatant fractions from TFA hydrolysis was determined by separation and quantitation of alditol acetates by gas liquid chromatography-mass spectrometry. In brief, the TFA was evaporated in a stream of nitrogen gas in the presence of *tert*-butyl alcohol to minimize destruction in concentrated acid and monosaccharides were reduced with NaBH$_4$ and then acetylated with acetic anhydride (Gibeaut and Carpita, 1991). The derivatives were separated into seven components representing the major sugars in plant cell walls by gas liquid chromatography on an SP-2330 (Supelco) using a 0.25-mm × 30-m column with temperatures from 80°C to 170°C, increased to 25°C min^{-1} followed by an increase of 5°C min^{-1} up to 240°C and a helium flow of 1 mL min^{-1}. Electron impact mass spectrometry was carried out on a Hewlett-Packard MSD at 70 eV with a source temperature of 250°C. Area under the curve calculations for each sugar derivative were scaled to μg per mg of sample tissue using the *myo*-inositol internal standard (Carpita and Shea, 1989).

Statistical Analysis

One-way ANOVA with Tukey's post-hoc tests were performed in SPSS (version 25) to determine significance among different treatments. Two-tailed Student's t test was performed in Excel 15.32.

For statistical analysis by X-bar and S Control Chart, the upper control limit (UCL) was calculated in Excel 15.32 using the following equation (Montgomery, 2009):

$$UCL = \overline{\bar{x} + 2\left(\frac{\bar{s}}{c_4\sqrt{n}}\right)}$$

Any value higher than the UCL was considered significantly different, with a P value < 0.05.

Accession Numbers

Sequence data from this article can be found in the Arabidopsis Genome Initiative under the following accession numbers: *MYOSIN XIK*, At5g20490; *MYOSIN XI1*, At1g17580; and *MYOSIN XI2*, At5g43900.

Supplemental Data

The following supplemental materials are available.

Supplemental Figure S1. Cellulose content is reduced in BDM-treated seedlings.

Supplemental Figure S2. Distribution of individual Golgi velocities following treatment with myosin inhibitors.

Supplemental Figure S3. PBP treatment reduces Golgi and MYOSIN XIK motility in a dose- and time-dependent manner and is reversible.

Supplemental Figure S4. PBP inhibits cytoplasmic streaming in *Chara corallina* internodal cells.

Supplemental Figure S5. Disruption of myosin does not cause clustering of CESA-containing Golgi.

Supplemental Figure S6. Selected regions of interest from control and inhibitor-treated cells have the same density of PM-localized CSCs at the beginning of FRAP experiments.

Supplemental Figure S7. Disruption of cortical microtubules does not alter the rate of CSC delivery to the PM.

Supplemental Figure S8. Inhibition of myosin activity reduces delivery of PIN2-GFP and BRI-GFP to the PM and leads to retention of intracellular secGFP.

Supplemental Figure S9. Velocity of CESA compartments is reduced in both cortical and subcortical cytoplasm of myosin-deficient cells.

Supplemental Figure S10. Internalization of FM4-64 and FLS2 is inhibited in myosin-deficient cells.

Supplemental Figure S11. Actin architecture in the cortical and subcortical cytoplasm of *xi3KO* mutant and myosin inhibitor-treated cells is altered.

Supplemental Figure S12. Inhibition of myosin results in accumulation of SYP61 vesicles in the cortical cytoplasm.

Supplemental Figure S13. Inhibition of myosin does not affect the microtubule-dependent positioning of CSC insertion sites.

Supplemental Figure S14. MYOSIN XIK and CESA6 transiently colocalize at CESA6 insertion sites.

Supplemental Table S1. Cell wall monosaccharide composition of wild-type, *xi3KO* mutant, and LatB-treated seedlings.

Supplemental Table S2. Summary of parameters affected by genetic or chemical disruption of plant myosin XI.

Supplemental Movie S1. Myosin inhibitor treatments reduce Golgi motility.

Supplemental Movie S2. Myosin inhibitor treatments reduce MYOSIN XIK motility.

Supplemental Movie S3. Small CESA compartments accumulate in the cortical cytoplasm of myosin- and actin-deficient cells.

Supplemental Movie S4. A successful CSC insertion event at the PM.

Supplemental Movie S5. A CSC particle is inserted next to a cortical microtubule and then migrates along the microtubule.

Supplemental Movie S6. A failed CSC insertion event that had a short pausing time at the PM.

Supplemental Movie S7. A failed CSC insertion event that had a long pausing time at the PM.

Supplemental Movie S8. MYOSIN XIK-YFP and tdTomato-CESA6 colocalize at CESA6 insertion site.

ACKNOWLEDGMENTS

LITERATURE CITED

Abu-Abied M, Belausov E, Hagay S, Peremyslov V, Dolja V, Sadot E (2018) Myosin XI-K is involved in root organogenesis, polar auxin transport, and cell division. J Exp Bot **69:** 2869–2881

Akkerman M, Overdijk EJ, Schel JH, Emons AM, Ketelaar T (2011) Golgi body motility in the plant cell cortex correlates with actin cytoskeleton organization. Plant Cell Physiol **52:** 1844–1855

Avisar D, Abu-Abied M, Belausov E, Sadot E (2012) Myosin XIK is a major player in cytoplasm dynamics and is regulated by two amino acids in its tail. J Exp Bot **63:** 241–249

Bashline L, Li S, Anderson CT, Lei L, Gu Y (2013) The endocytosis of cellulose synthase in Arabidopsis is dependent on μ2, a clathrin-mediated endocytosis adaptin. Plant Physiol **163:** 150–160

Bashline L, Li S, Gu Y (2014) The trafficking of the cellulose synthase complex in higher plants. Ann Bot **114:** 1059–1067

Bashline L, Li S, Zhu X, Gu Y (2015) The TWD40-2 protein and the AP2 complex cooperate in the clathrin-mediated endocytosis of cellulose synthase to regulate cellulose biosynthesis. Proc Natl Acad Sci USA **112:** 12870–12875

Beck M, Zhou J, Faulkner C, MacLean D, Robatzek S (2012) Spatio-temporal cellular dynamics of the *Arabidopsis* flagellin receptor reveal activation status-dependent endosomal sorting. Plant Cell **24:** 4205–4219

Bringmann M, Li E, Sampathkumar A, Kocabek T, Hauser M-T, Persson S (2012) POM-POM2/cellulose synthase interacting1 is essential for the functional association of cellulose synthase and microtubules in *Arabidopsis.* Plant Cell **24:** 163–177

Cai C, Henty-Ridilla JL, Szymanski DB, Staiger CJ (2014) Arabidopsis myosin XI: A motor rules the tracks. Plant Physiol **166:** 1359–1370

Carpita NC, Shea EM (1989) Linkage structure of carbohydrates by gas chromatography-mass spectrometry (GC-MS) of partially methylated alditol acetates. *In* CJ Biermann, GD McGinnis, eds, Analysis of Carbohydrates by GLC and MS. CRC Press, Boca Raton, FL, pp 157–174

Crowell EF, Bischoff V, Desprez T, Rolland A, Stierhof Y-DD, Schumacher K, Gonneau M, Höfte H, Vernhettes S (2009) Pausing of Golgi bodies on microtubules regulates secretion of cellulose synthase complexes in *Arabidopsis.* Plant Cell **21:** 1141–1154

Delmer DP (1999) Cellulose biosynthesis: Exciting times for a difficult field of study. Annu Rev Plant Physiol Plant Mol Biol **50:** 245–276

Dettmer J, Hong-Hermesdorf A, Stierhof Y-D, Schumacher K (2006) Vacuolar H+-ATPase activity is required for endocytic and secretory trafficking in *Arabidopsis.* Plant Cell **18:** 715–730

Diotallevi F, Mulder B (2007) The cellulose synthase complex: A polymerization driven supramolecular motor. Biophys J **92:** 2666–2673

Donovan KW, Bretscher A (2012) Myosin-V is activated by binding secretory cargo and released in coordination with Rab/exocyst function. Dev Cell **23:** 769–781

Donovan KW, Bretscher A (2015) Tracking individual secretory vesicles during exocytosis reveals an ordered and regulated process. J Cell Biol **210:** 181–189

Drakakaki G, van de Ven W, Pan S, Miao Y, Wang J, Keinath NF, Weatherly B, Jiang L, Schumacher K, Hicks G, Raikhel N (2012) Isolation and proteomic analysis of the SYP61 compartment reveal its role in exocytic trafficking in *Arabidopsis.* Cell Res **22:** 413–424

Dubois M, Gilles KA, Hamilton JK, Rebers P, Smith F (1956) Colorimetric method for determination of sugars and related substances. Anal Chem **28:** 350–356

Fagard M, Desnos T, Desprez T, Goubet F, Refregier G, Mouille G, McCann M, Rayon C, Vernhettes S, Höfte H (2000) PROCUSTE1 encodes a cellulose synthase required for normal cell elongation specifically in roots and dark-grown hypocotyls of Arabidopsis. Plant Cell **12:** 2409–2424

Falbel TG, Koch LM, Nadeau JA, Segui-Simarro JM, Sack FD, Bednarek SY (2003) SCD1 is required for cytokinesis and polarized cell expansion in *Arabidopsis thaliana* [corrected]. Development **130:** 4011–4024

Fedorov R, Böhl M, Tsiavaliaris G, Hartmann FK, Taft MH, Baruch P, Brenner B, Martin R, Knölker H-J, Gutzeit HO, Manstein DJ (2009) The mechanism of pentabromopseudilin inhibition of myosin motor activity. Nat Struct Mol Biol **16:** 80–88

Fendrych M, Synek L, Pecenková T, Toupalová H, Cole R, Drdová E, Nebesárová J, Sedinová M, Hála M, Fowler JE, Zársky V (2010) The *Arabidopsis* exocyst complex is involved in cytokinesis and cell plate maturation. Plant Cell **22:** 3053–3065

Foth BJ, Goedecke MC, Soldati D (2006) New insights into myosin evolution and classification. Proc Natl Acad Sci USA **103:** 3681–3686

Funaki K, Nagata A, Akimoto Y, Shimada K, Ito K, Yamamoto K (2004) The motility of *Chara corallina* myosin was inhibited reversibly by 2,3-butanedione monoxime (BDM). Plant Cell Physiol **45:** 1342–1345

Geldner N, Hyman DL, Wang X, Schumacher K, Chory J (2007) Endosomal signaling of plant steroid receptor kinase BRI1. Genes Dev 21: 1598–1602

Gibeaut DM, Carpita NC (1991) Tracing cell wall biogenesis in intact cells and plants: Selective turnover and alteration of soluble and cell wall polysaccharides in grasses. Plant Physiol 97: 551–561

Giddings TH, Jr., Brower DL, Staehelin LA (1980) Visualization of particle complexes in the plasma membrane of Micrasterias denticulata associated with the formation of cellulose fibrils in primary and secondary cell walls. J Cell Biol 84: 327–339

Gutierrez R, Lindeboom JJ, Paredez AR, Emons AM, Ehrhardt DW (2009) Arabidopsis cortical microtubules position cellulose synthase delivery to the plasma membrane and interact with cellulose synthase trafficking compartments. Nat Cell Biol 11: 797–806

Gutiérrez LM (2012) New insights into the role of the cortical cytoskeleton in exocytosis from neuroendocrine cells. Int Rev Cell Mol Biol 295: 109–137

Haigler CH, Brown RM Jr (1986) Transport of rosettes from the Golgi apparatus to the plasma membrane in isolated mesophyll cells of Zinnia elegans during differentiation to tracheary elements in suspension culture. Protoplasma 134: 111–120

Hála M, Cole R, Synek L, Drdová E, Pecenková T, Nordheim A, Lamkemeyer T, Madlung J, Hochholdinger F, Fowler JE, Zárský V (2008) An exocyst complex functions in plant cell growth in Arabidopsis and tobacco. Plant Cell 20: 1330–1345

Heard W, Sklenář J, Tomé DF, Robatzek S, Jones AM (2015) Identification of regulatory and cargo proteins of endosomal and secretory pathways in Arabidopsis thaliana by proteomic dissection. Mol Cell Proteomics 14: 1796–1813

Henty JL, Bledsoe SW, Khurana P, Meagher RB, Day B, Blanchoin L, Staiger CJ (2011) Arabidopsis actin depolymerizing factor4 modulates the stochastic dynamic behavior of actin filaments in the cortical array of epidermal cells. Plant Cell 23: 3711–3726

Higaki T, Kutsuna N, Sano T, Kondo N, Hasezawa S (2010) Quantification and cluster analysis of actin cytoskeletal structures in plant cells: role of actin bundling in stomatal movement during diurnal cycles in Arabidopsis guard cells. Plant J 61: 156–165

Islam K, Chin HF, Olivares AO, Saunders LP, De La Cruz EM, Kapoor TM (2010) A myosin V inhibitor based on privileged chemical scaffolds. Angew Chem Int Ed Engl 49: 8484–8488

Jin Y, Sultana A, Gandhi P, Franklin E, Hamamoto S, Khan AR, Munson M, Schekman R, Weisman LS (2011) Myosin V transports secretory vesicles via a Rab GTPase cascade and interaction with the exocyst complex. Dev Cell 21: 1156–1170

Lauber MH, Waizenegger I, Steinmann T, Schwarz H, Mayer U, Hwang I, Lukowitz W, Jürgens G (1997) The Arabidopsis KNOLLE protein is a cytokinesis-specific syntaxin. J Cell Biol 139: 1485–1493

Lei L, Singh A, Bashline L, Li S, Yingling YG, Gu Y (2015) CELLULOSE SYNTHASE INTERACTIVE1 is required for fast recycling of cellulose synthase complexes to the plasma membrane in Arabidopsis. Plant Cell 27: 2926–2940

Li J, Blanchoin L, Staiger CJ (2015) Signaling to actin stochastic dynamics. Annu Rev Plant Biol 66: 415–440

Li S, Lei L, Somerville CR, Gu Y (2012) Cellulose synthase interactive protein 1 (CSI1) links microtubules and cellulose synthase complexes. Proc Natl Acad Sci USA 109: 185–190

Li S, Bashline L, Zheng Y, Xin X, Huang S, Kong Z, Kim SH, Cosgrove DJ, Gu Y (2016) Cellulose synthase complexes act in a concerted fashion to synthesize highly aggregated cellulose in secondary cell walls of plants. Proc Natl Acad Sci USA 113: 11348–11353

Luo Y, Scholl S, Doering A, Zhang Y, Irani NG, Rubbo SD, Neumetzler L, Krishnamoorthy P, Van Houtte I, Mylle E, et al (2015) V-ATPase activity in the TGN/EE is required for exocytosis and recycling in Arabidopsis. Nat Plants 1: 15094

Luschnig C, Vert G (2014) The dynamics of plant plasma membrane proteins: PINs and beyond. Development 141: 2924–2938

Madison SL, Buchanan ML, Glass JD, McClain TF, Park E, Nebenführ A (2015) Class XI myosins move specific organelles in pollen tubes and are required for normal fertility and pollen tube growth in Arabidopsis. Plant Physiol 169: 1946–1960

Mao H, Nakamura M, Viotti C, Grebe M (2016) A framework for lateral membrane trafficking and polar tethering of the PEN3 ATP-binding cassette transporter. Plant Physiol 172: 2245–2260

Maschi D, Gramlich MW, Klyachko VA (2018) Myosin V functions as a vesicle tether at the plasma membrane to control neurotransmitter release in central synapses. eLife 7: e39440

Mayers JR, Hu T, Wang C, Cárdenas JJ, Tan Y, Pan J, Bednarek SY (2017) SCD1 and SCD2 form a complex that functions with the exocyst and RabE1 in exocytosis and cytokinesis. Plant Cell 29: 2610–2625

McCurdy DW (1999) Is 2,3-butanedione monoxime an effective inhibitor of myosin-based activities in plant cells? Protoplasma 209: 120–125

McFarlane HE, Döring A, Persson S (2014) The cell biology of cellulose synthesis. Annu Rev Plant Biol 65: 69–94

Meijering E, Dzyubachyk O, Smal I (2012) Methods for cell and particle tracking. Methods Enzymol 504: 183–200

Montgomery DC (2009) Introduction to Statistical Quality Control. John Wiley & Sons, New York

Nebenführ A, Gallagher LA, Dunahay TG, Frohlick JA, Mazurkiewicz AM, Meehl JB, Staehelin LA (1999) Stop-and-go movements of plant Golgi stacks are mediated by the acto-myosin system. Plant Physiol 121: 1127–1142

Nightingale TD, Cutler DF, Cramer LP (2012) Actin coats and rings promote regulated exocytosis. Trends Cell Biol 22: 329–337

Ojangu E-L, Tanner K, Pata P, Järve K, Holweg CL, Truve E, Paves H (2012) Myosins XI-K, XI-1, and XI-2 are required for development of pavement cells, trichomes, and stigmatic papillae in Arabidopsis. BMC Plant Biol 12: 81

Paredez AR, Somerville CR, Ehrhardt DW (2006) Visualization of cellulose synthase demonstrates functional association with microtubules. Science 312: 1491–1495

Park E, Nebenführ A (2013) Myosin XIK of Arabidopsis thaliana accumulates at the root hair tip and is required for fast root hair growth. PLoS One 8: e76745

Peremyslov VV, Prokhnevsky AI, Avisar D, Dolja VV (2008) Two class XI myosins function in organelle trafficking and root hair development in Arabidopsis. Plant Physiol 146: 1109–1116

Peremyslov VV, Prokhnevsky AI, Dolja VV (2010) Class XI myosins are required for development, cell expansion, and F-Actin organization in Arabidopsis. Plant Cell 22: 1883–1897

Peremyslov VV, Klocko AL, Fowler JE, Dolja VV (2012) Arabidopsis myosin XI-K localizes to the motile endomembrane vesicles associated with F-actin. Front Plant Sci 3: 184

Perico C, Sparkes I (2018) Plant organelle dynamics: Cytoskeletal control and membrane contact sites. New Phytol 220: 381–394

Prokhnevsky AI, Peremyslov VV, Dolja VV (2008) Overlapping functions of the four class XI myosins in Arabidopsis growth, root hair elongation, and organelle motility. Proc Natl Acad Sci USA 105: 19744–19749

Qi X, Kaneda M, Chen J, Geitmann A, Zheng H (2011) A specific role for Arabidopsis TRAPPII in post-Golgi trafficking that is crucial for cytokinesis and cell polarity. Plant J 68: 234–248

Reddy AS, Day IS (2001) Analysis of the myosins encoded in the recently completed Arabidopsis thaliana genome sequence. Genome Biol 2: H0024

Robert S, Chary SN, Drakakaki G, Li S, Yang Z, Raikhel NV, Hicks GR (2008) Endosidin1 defines a compartment involved in endocytosis of the brassinosteroid receptor BRI1 and the auxin transporters PIN2 and AUX1. Proc Natl Acad Sci USA 105: 8464–8469

Ryan JM, Nebenführ A (2018) Update on myosin motors: Molecular mechanisms and physiological functions. Plant Physiol 176: 119–127

Sampathkumar A, Gutierrez R, McFarlane HE, Bringmann M, Lindeboom J, Emons A-MM, Samuels L, Ketelaar T, Ehrhardt DW, Persson S (2013) Patterning and lifetime of plasma membrane-localized cellulose synthase is dependent on actin organization in Arabidopsis interphase cells. Plant Physiol 162: 675–688

Sánchez-Rodríguez C, Shi Y, Kesten C, Zhang D, Sancho-Andrés G, Ivakov A, Lampugnani ER, Sklodowski K, Fujimoto M, Nakano A, et al (2018) The cellulose synthases are cargo of the TPLATE adaptor complex. Mol Plant 11: 346–349

Sattarzadeh A, Schmelzer E, Hanson MR (2013) Arabidopsis myosin XI sub-domains homologous to the yeast myo2p organelle inheritance subdomain target subcellular structures in plant cells. Front Plant Sci 4: 407

Schindelin J, Arganda-Carreras I, Frise E, Kaynig V, Longair M, Pietzsch T, Preibisch S, Rueden C, Saalfeld S, Schmid B, et al (2012) Fiji: An open-source platform for biological-image analysis. Nat Methods 9: 676–682

Shaw SL, Kamyar R, Ehrhardt DW (2003) Sustained microtubule treadmilling in Arabidopsis cortical arrays. Science 300: 1715–1718

Shimmen T, Yokota E (2004) Cytoplasmic streaming in plants. Curr Opin Cell Biol **16:** 68–72

Smith JM, Leslie ME, Robinson SJ, Korasick DA, Zhang T, Backues SK, Cornish PV, Koo AJ, Bednarek SY, Heese A (2014) Loss of *Arabidopsis thaliana* Dynamin-Related Protein 2B reveals separation of innate immune signaling pathways. PLoS Pathog **10:** e1004578

Somerville C (2006) Cellulose synthesis in higher plants. Annu Rev Cell Dev Biol **22:** 53–78

Synek L, Sekereš J, Žárský V (2014) The exocyst at the interface between cytoskeleton and membranes in eukaryotic cells. Front Plant Sci **4:** 543

Tominaga M, Yokota E, Sonobe S, Shimmen T (2000) Mechanism of inhibition of cytoplasmic streaming by a myosin inhibitor, 2,3-butanedione monoxime. Protoplasma **213:** 46–54

Tominaga M, Kimura A, Yokota E, Haraguchi T, Shimmen T, Yamamoto K, Nakano A, Ito K (2013) Cytoplasmic streaming velocity as a plant size determinant. Dev Cell **27:** 345–352

Toyooka K, Goto Y, Asatsuma S, Koizumi M, Mitsui T, Matsuoka K (2009) A mobile secretory vesicle cluster involved in mass transport from the Golgi to the plant cell exterior. Plant Cell **21:** 1212–1229

Ueda H, Yokota E, Kutsuna N, Shimada T, Tamura K, Shimmen T, Hasezawa S, Dolja VV, Hara-Nishimura I (2010) Myosin-dependent endoplasmic reticulum motility and F-actin organization in plant cells. Proc Natl Acad Sci USA **107:** 6894–6899

Ueda H, Tamura K, Hara-Nishimura I (2015) Functions of plant-specific myosin XI: From intracellular motility to plant postures. Curr Opin Plant Biol **28:** 30–38

Updegraff DM (1969) Semimicro determination of cellulose in biological materials. Anal Biochem **32:** 420–424

Viotti C, Bubeck J, Stierhof Y-DD, Krebs M, Langhans M, van den Berg W, van Dongen W, Richter S, Geldner N, Takano J, , et al (2010) Endocytic and secretory traffic in *Arabidopsis* merge in the trans-Golgi network/early endosome, an independent and highly dynamic organelle. Plant Cell **22:** 1344–1357

Vukašinović N, Oda Y, Pejchar P, Synek L, Pečenková T, Rawat A, Sekereš J, Potocký M, Žárský V (2017) Microtubule-dependent targeting of the exocyst complex is necessary for xylem development in Arabidopsis. New Phytol **213:** 1052–1067

Waizenegger I, Lukowitz W, Assaad F, Schwarz H, Jürgens G, Mayer U (2000) The *Arabidopsis* KNOLLE and KEULE genes interact to promote vesicle fusion during cytokinesis. Curr Biol **10:** 1371–1374

Wallace IS, Somerville CR (2015) A blueprint for cellulose biosynthesis, deposition, and regulation in plants. *In* H Fukuda, ed, Plant Cell Wall Patterning and Cell Shape. Wiley, Hoboken, NJ, pp 65–97

Xu J, Scheres B (2005) Dissection of Arabidopsis ADP-RIBOSYLATION FACTOR 1 function in epidermal cell polarity. Plant Cell **17:** 525–536

Yamamoto K, Kikuyama M, Sutoh-Yamamoto N, Kamitsubo E (1994) Purification of actin based motor protein from *Chara corallina*. Proc Jpn Acad **70:** 175–180

Yang L, Qin L, Liu G, Peremyslov VV, Dolja VV, Wei Y (2014) Myosins XI modulate host cellular responses and penetration resistance to fungal pathogens. Proc Natl Acad Sci USA **111:** 13996–14001

Zhang X, Henriques R, Lin S-S, Niu Q-W, Chua N-H (2006) *Agrobacterium*-mediated transformation of *Arabidopsis thaliana* using the floral dip method. Nat Protoc **1:** 641–646

Zheng H, Kunst L, Hawes C, Moore I (2004) A GFP-based assay reveals a role for RHD3 in transport between the endoplasmic reticulum and Golgi apparatus. Plant J **37:** 398–414

Zhu X, Li S, Pan S, Xin X, Gu Y (2018) CSI1, PATROL1, and exocyst complex cooperate in delivery of cellulose synthase complexes to the plasma membrane. Proc Natl Acad Sci USA **115:** E3578–E3587